Journal of Energy Chemistry 59 (2021) 547–571

Contents lists available at ScienceDirect

Journal of Energy Chemistry

journal homepage: www.elsevier.com/locate/jechem

http://www.journals.elsevier.com/journal-of-energy-chemistry/

Review

Nanostructured Mn-based oxides as high-performance cathodes for next generation Li-ion batteries

Guodong Hao [a], Qinzhi Lai [b,*], Hongzhang Zhang [c,*]

[a] School of Chemistry and Chemical Engineering, Mudanjiang Normal University, Mudanjiang 157011, Heilongjiang, China
[b] Department of Chemistry, College of Sciences, Northeastern University, Shenyang 110819, Liaoning, China
[c] Division of Energy Storage, Dalian Institute of Chemical Physics, Chinese Academy of Sciences, Dalian 116023, Liaoning, China

ARTICLE INFO

Article history:
Received 18 October 2020
Revised 20 November 2020
Accepted 30 November 2020
Available online 11 December 2020

Keywords:
Mn-based oxide
Cathode material
Electrochemical property
Modification

ABSTRACT

Mn-based oxides have been regarded as a promising family of cathode materials for high-performance lithium-ion batteries, but the practical applications have been limited because of severe capacity deterioration (such as $LiMnO_2$ and $LiMn_2O_4$) as well as further complications from successive structure changes during cycling, low initial coulombic efficiency (such as Li-rich cathode) and oxidization of organic carbonate solvents at high charge potential (such as $LiNi_{0.5}Mn_{1.5}O_4$). Large amounts of efforts have been concentrated on resolving these issues towards practical applications, and many vital progresses have been carried out. Hence, the primary target of this review is focused on different proposed strategies and breakthroughs to enhance the rate performance and cycling stability of nanostructured Mn-based oxide cathode materials for Li-ion batteries, including morphology control, ion doping, surface coatings, composite construction. The combination of delicate architectures with conductive species represents the perspective ways to enhance the conductivity of the cathode materials and further buffer the structure transformation and strain during cycling. At last, based on the elaborated progress, several perspectives of Mn-based oxide cathodes are summarized, and some possible attractive strategies and future development directions of Mn-based oxide cathodes with enhanced electrochemical properties are proposed. The review will offer a detailed introduction of various strategies enhancing electrochemical performance and give a novel viewpoint to shed light on the future innovation in Mn-based oxide cathode materials, which benefits the design and construction of high-performance Mn-based oxide cathode materials in the future.

Contents

* Corresponding authors.
E-mail addresses: qinzhi1226@163.com (Q. Lai), zhanghz@dicp.ac.cn (H. Zhang).

https://doi.org/10.1016/j.jechem.2020.11.035

Guodong Hao is currently a full professor of Mudanjiang Normal University. He received his Ph.D. degree in Chemical Engineering and Technology from Harbin Institute of Technology in 2008. He has published more than 20 papers in peer-reviewed journals as the first author or corresponding author. His research interests mainly focus on the synthesis and characterization of functional materials.

Qinzhi Lai received his B.S. and Ph. D. degrees from Harbin Institute of Technology in 2004 and 2009, respectively. He joined the Dalian Institute of Chemical Physics, Chinese Academy of Sciences as an associate research fellow in 2009. He is currently an associate professor in the Northeastern University at Qinhuangdao. His current research interest is advanced electrode materials for energy storage devices.

Hongzhang Zhang is currently a professor in the Division of Energy Storage, Dalian Institute of Chemical Physics, Chinese Academy of Sciences. He received his B. S. degree from Shandong University in 2008. He received his Ph.D. degree from University of Chinese Academy of Science in 2013. His research interests focus on the development of novel batteries with high energy density.

1. Introduction

Li-ion batteries (LIBs) have been considered as one of the most hopeful energy storage technologies because of the high voltage, excellent cycling stability and environment friendly nature [1,2]. Unfortunately, the large-scale application of LIBs to power EVs (electric vehicles) or HEVs (hybrid electric vehicles) are observably impeded by some main technical obstacles, such as low power density, high cost and poor safety characteristics. As we know, the electrochemical property of Li-ion batteries is principally decided by the electrode materials. Actually, cathode materials act a vital role in the determination of capacity, battery voltage, energy density, safety and cycle life of LIBs. In addition, the cathode material for the full battery costs by 40%. Until now, four main types of cathode materials have been studied intensively, i.e. layered transition metal oxides (TMOs), Mn-based oxide spinels, phosphate and silicate materials [3–6]. Among all cathode materials, Mn-based oxide cathodes have been paid much attention due to their large nature abundance, low cost as well as different crystal structures and phases [7–12]. For instance, spinel $LiNi_{0.5}Mn_{1.5}O_4$ shows a high energy density of 650 Wh kg^{-1} due to its high operating voltage of 4.7 V, which is higher than some commercialized cathode material, such as $LiCoO_2$, $LiFePO_4$ and $LiCo_{1/3}Ni_{1/3}Mn_{1/3}O_2$ [13]. The layered Mn-based Li-rich materials can deliver excellent reversible capacity of ~280 mAh g^{-1}, and then shows high energy density of about 900 Wh kg^{-1} [3]. Unfortunately, several challenges still need to be resolved for Mn-based cathode materials before large-scale applications, including the Mn dissolution for $LiMnO_2$, $LiMn_2O_4$, $LiMnPO_4$ and $LiMn_2SiO_4$ due to the Jahn-Teller effect [14–16] and poor initial coulombic efficiency, electrolyte decomposition for Mn-based Li rich materials and $LiNi_{0.5}Mn_{1.5}O_4$ due to the high charge voltage [17,18]. The Jahn-Teller theorem essentially states that any nonlinear molecule with a spatially degenerate electronic ground state will undergo a geometrical distortion that removes that degeneracy, because the distortion lowers the overall energy of the species. Such a theorem can also be applied to descript the geometrical distortion that occurs in crystals. Mn^{3+} ion has a high-spin d^4 configuration, which is clearly typically Jahn-Teller active. For Mn^{3+} ions in MO_6 octahedrons, the high and low spin arrangements are $t_{2g}^3e_g^1$ and t_{2g}^4 respectively, which result in odd number of electrons in e_g and t_{2g} orbitals respectively and thus the occurrence of the Jahn-Teller effect. It induces two long bond lengths along the *z*-axis direction and four short bond lengths in the *xy*-plane or two short bond lengths along the *z*-axis direction and four long bond lengths in the *xy*-plane [16]. The Jahn-Teller effect induced volume and cell distortion of the electrode, and then resulted in a rapid mechanical degradation of the electrode. Hence, numerous strategies have been used to conquer these challenges, including surface modification, doping, construction nanostructure with unique morphology. The lattice doping can alleviate the Jahn-Teller effect, and then restrain Mn dissolution. Surface coating can reduce the direct contact between Mn-based cathodes and electrolyte, and then restrain side reaction between cathode and electrolyte.

Compared with bulk cathode materials, nanostructured cathode materials show a lot of structure-dependent superiorities due to the characteristics including high surface-to-mass/volume ratio, diminutive building blocks, enhanced accommodation of the strain and robust secondary configuration. The high surface area can provide more active sites for electrochemical reaction and promote the electrolyte diffusion. The small-sized particles can shorten transfer path of ions and electrons, and then promote the ion or electron transport kinetic performance [18,19]. In addition, the electrochemical performance of nanostructured cathode materials can be further enhanced by tailoring their size, morphology, and composition. All these characteristics of nanostructure usually effectively enhance the reversible capacity and cycle performance of cathode materials even at large current densities. Although some reviews of these Mn-based oxides as cathode materials are continually emerging, most reviews only focus on a single compound or material, such as Mn-based Li-rich materials, $LiMn_2O_4$, $LiNi_{0.5}Mn_{1.5}O_4$. Apparently, the review articles mentioned above do not cover the new development of Mn-based oxide cathodes. As far as we know, a critical review that deeply emphasizes on the electrochemical performances of various Mn-based oxides as cathode materials of Li-ion batteries, such as $LiMnO_2$, Mn-based Li-rich materials, $LiMn_2O_4$, $LiNi_{0.5}Mn_{1.5}O_4$ has not yet been reported. Hence, the primary target of this review is focused on different proposed strategies and breakthroughs to enhance the rate performance and cycling stability of nanostructured Mn-based oxide cathode materials for LIBs, including morphology control, surface coatings, composite construction, ion doping. Each strategy has its relative merits and disadvantages. The traditional morphology control is based on various nanostructures including 1D (one-dimensional) nanofiber (or nanorods, nanotubes, nanowires), 2D (two dimensional) nanosheet (nanoplate) and 3D (three-dimensional) microstructure composed of 1D or 2D nanostructures. The morphology control can reduce the transmission pathway of lithium ions and electrons based on the ion diffusion equation, and then improve the electrochemical performance of electrode materials. However, the intrinsic low conductivity of electrode materials for LIBs usually results in high polarization cycled at high current densities. In addition, the electrode materials suffer from the aggressive electrolyte oxidation at the later stage of charging and the transitional metals dissolution in the

HF-containing electrolyte, resulting in serious structure deterioration. Surface coating or composite construction with a conductive layer is an effective strategy to improve the conductivity of electrode materials and interfacial stability between electrode and electrolyte, which can reduce the direct contact between electrode materials and electrolyte, and then restrain side reaction between cathode and electrolyte. However, a uniform surface coating around the whole particle of electrode materials is difficult to achieve. Fortunately, element doping has been proved to be an efficient strategy to enhance the inherent conductivity of electrode materials. The doping can alter the bond strength, the local environment of the lattice, the valence state of cations, and then the lattice defect may be introduced. Doping can also purposefully create gaps or alter the size of channels by enhancing the stability of the primary skeleton, or alter ion inter-atomic forces to promote the ions transmission, then enhances the conductivity of electrode materials [1]. A combination between morphology control and surface coatings, composite construction, ion doping may be a more effective strategy to achieve deeper insight into the structure-performance issues, which contribute to the rational design and structure optimization of Mn-based cathode materials. At last, an insight into the future development directions of manganese-based oxide cathodes is proposed. The review will offer a scientific and detailed introduction of various enhancing strategies and give a novel viewpoint to shed light on the future innovation in Mn-based oxide cathode materials, which benefits their design and construction of high-performance Mn-based oxide cathode materials in the future.

2. Nanostructured $LiMnO_2$ cathode material

$LiMnO_2$ is a homogeneous polycrystalline compound, which has three structures (Fig. 1a): Orthorhombic, monoclinic and rhombohedral structures with space group Pmnm, C2/m and R3-m, respectively. Orthorhombic $LiMnO_2$ belongs to the orthorhombic crystal system and its space group is Pmnm. It is usually abbreviated as o-$LiMnO_2$. In the crystal, LiO_6 and MnO_6 octahedrons are arranged alternatively, and the shift of Mn^{3+} towards lithium layer leads to a Jahn-Teller distortion effect, which elongates the MnO_6 octahedron framework by 14%. Monoclinic $LiMnO_2$ abbreviated as m-$LiMnO_2$ belongs to the monoclinic crystal system, and it has an α-$NaFeO_2$ type structure, which is like that of $LiCoO_2$ and $LiNiO_2$. The space group of m-$LiMnO_2$ is C2/m, and it is stable in air and possesses a NaCl-type microscopic structure. In this structure, two different kinds of ions are arranged alternatively along the [110] direction. Tetragonal $LiMnO_2$ is represented as t-$LiMnO_2$ and it belongs to the tetragonal crystal system with a space group of $I_{41/amd}$. The distribution of the cations can be expressed as $[Li^+]_{8a}[Li^+]_{16c}[Mn_2^{3+}]_{16d}O_4^{2-}$. 8a site represents the tetrahedron position, while 6c and 16d sites are the octahedron ones. At present, the structure used as the cathode material for LIBs application is mainly the layered $LiMnO_2$. Based on the one-electron transfer

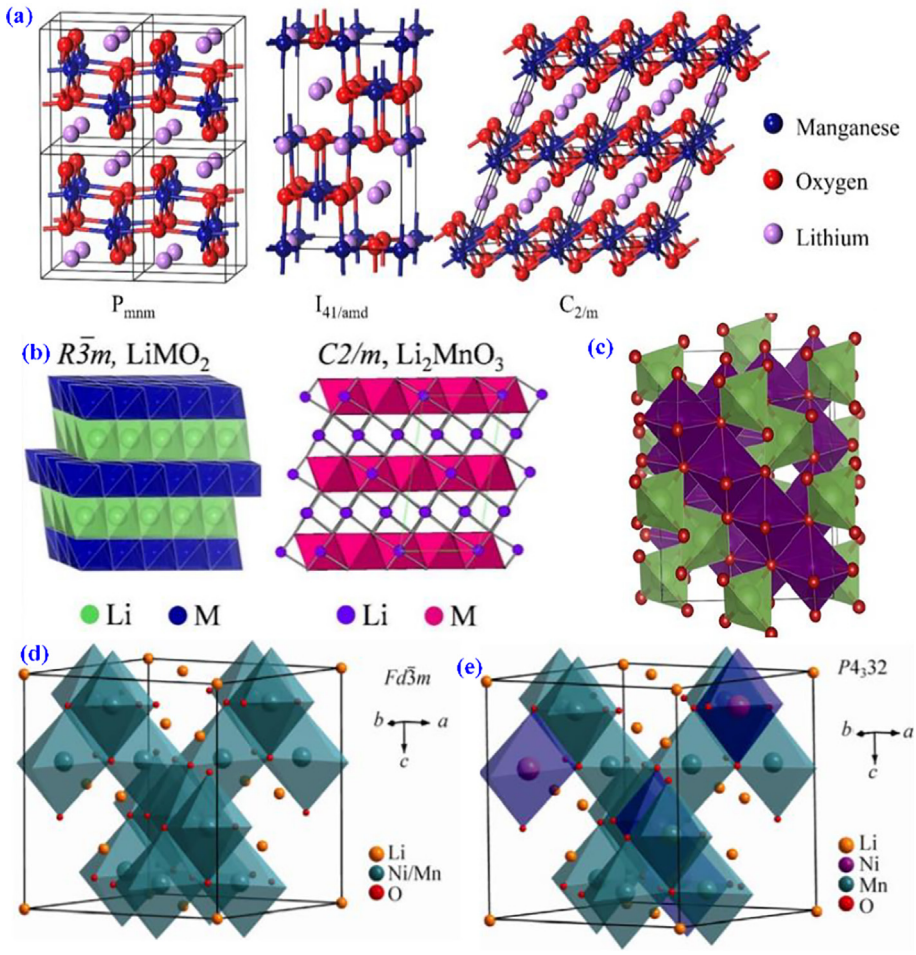

Fig. 1. Crystal structure of (a) $LiMnO_2$ with different space groups, (b) $LiMO_2$ and Li_2MnO_3 [8], (c) $LiMn_2O_4$ [11], $LiNi_{0.5}Mn_{1.5}O_4$ with (d) Fd-3 m and (e) $P4_332$ space groups [12]. Reproduced from Refs. [8,11,12] with permission from the American Chemical Society.

between Mn^{3+} and Mn^{4+}, the theoretical capacity of $LiMnO_2$ cycled between 2 and 4.5 V is 286 mAh g^{-1} [20]. The mechanism of capacity fading can be summarized as follows: (1) Mn dissolution form the disproportionation reaction of $2Mn^{3+} \rightarrow Mn^{2+}$ (electrolyte-soluble) Mn^{4+}; (2) oxygen evolution at $LiMnO_2$/electrolyte interface; (3) structure transformation to spinel phase.

The $LiMnO_2$ can be an ideal replacement with a large practical capacity of 200 mAh g^{-1} and low cost. Nevertheless, the awful cycling stability hinders the practical application [21]. Furthermore, the nanostructure has attracted much attention because of the larger specific surface and enhanced energy density [22]. Hence, effort has been devoted to the *o*-$LiMnO_2$ materials. Table 1 summarizes the crystallographic structure, morphology, synthesis method and cycle performance of several nanostructured *o*-$LiMnO_2$, and the corresponding SEM images are shown in Fig. 2.

The layered $LiMnO_2$ has been considered as a hopeful alternative to $LiCoO_2$ because of its large theoretical capacity, low cost, low toxicity, and high safety in overcharge conditions. Although $LiMnO_2$ has similar chemical formula to $LiCoO_2$, the structure is not identical to the layered O3-structure as it is easy to crystallize in an orthorhombic phase. In addition, the metastable layered phase gradually transforms into a highly disordered spinel-like $LiMn_2O_4$ during cycling because the layered $LiMnO_2$ rock salt structure is very similar to spinel. To resolve these issues, nanostructured metal ions-doped $LiM_xMn_{1-x}O_2$, such as Mn-based Li-rich phase ($xLi_2MnO_3 \cdot (1-x)LiMO_2$, M = transition metals) are proposed. The Mn-based Li-rich phase shows higher reversible capacity and cycling stability than those of $LiMnO_2$.

Table 1
Morphology, synthesis method and cycling performance of nanostructured *o*-$LiMnO_2$.

Morphology	Synthesis method	Electrochemical properties including initial specific capacity, capacity retention (cycles, rate, voltage range)	Ref.
Nanorods	Hydrothermal conversion	260 mAh g^{-1}, 66.9% (7, 1/20C, 2.0–4.5 V)	[23]
Nanorods	Hydrothermal route	148 mAh g^{-1}, 75% (30, 0.1C, 2.0–4.5 V)	[24]
Nanoplates	Hydrothermal route	235 mAh g^{-1} (second), 80.8% (20, 0.01 A g^{-1}, 2.0–4.5 V)	[25]
Nanospheres	Microwave-hydrothermal routine	228 mAh g^{-1}, 70.2% (50, 0.1C, 2.0–4.5 V)	[26]
Nano-particles	One-step hydrothermal method	138.2 mAh g^{-1}, 100% (30, 0.05C, 2.0–4.3 V)	[27]
Nano-particles	Hydrothermal method	166 mAh g^{-1}, >90.4% (6, 0.05C, 2.0–4.5 V)	[28]

3. Nanostructured Mn-based Li-rich cathode materials

Mn-based Li-rich compounds ($xLi_2MnO_3 \cdot (1-x)LiMO_2$, M = transition metals) can be considered as a composite between monoclinic Li_2MnO_3 (C2/m structure) and trigonal $LiMO_2$ (R-3 m structure) at the atomic level (Fig. 1b). Li_2MnO_3 can be denoted as $Li[Li_{1/3}Mn_{2/3}]O_2$, and then can be denoted as layered $LiMO_2$ compounds. It is an O3-type structure where interslab octahedral positions are only taken up by Li whereas slab octahedral positions are taken up by Li and Mn with a molar ratio of 1:2 [29]. Mn-based Li-rich compounds with a large practical capacity of about 250 mAh g^{-1} have been regarded as one of a hopeful cathode material with great promise. The Li_2MnO_3 component can provide additional lithium ions at potentials higher than 4.50 V, resulting in the improvement of working voltage and thermodynamic stability [30]. To show the complicated electrochemical reaction mechanisms of Mn-based Li-rich electrode, a schematic diagram of structure change for $Li_2MnO_3 \cdot LiCo_{1/3}Mn_{1/3}Ni_{1/3}O_2$ during the initial cycle is systematically given in Fig. 3 by Yi et al. [31].

The charge mechanism below 4.40 V at the first cycle is as follows:

$$xLi_2MnO_3 \cdot (1-x)LiCo_{1/3}Mn_{1/3}Ni_{1/3}O_2 \overset{\text{Charge}}{\rightarrow} xLi_2MnO_3 \cdot Co_{1/3}Mn_{1/3}Ni_{1/3}O_2 + (1-x)Li^+ + (1-x)e^- \quad (1)$$

As shown in Fig. 3(a), Li^+ ion is taken off from the $LiCo_{1/3}Mn_{1/3}Ni_{1/3}O_2$ along with the oxidation of Ni ions from Ni^{2+} to Ni^{4+} and Co ions from Co^{2+} to Co^{3+}. However, Li_2MnO_3 does not exhibit electrochemical activity because Li^+ ions are difficult to enter the manganese layer. When the charging voltage exceeds 4.40 V, Li_2MnO_3

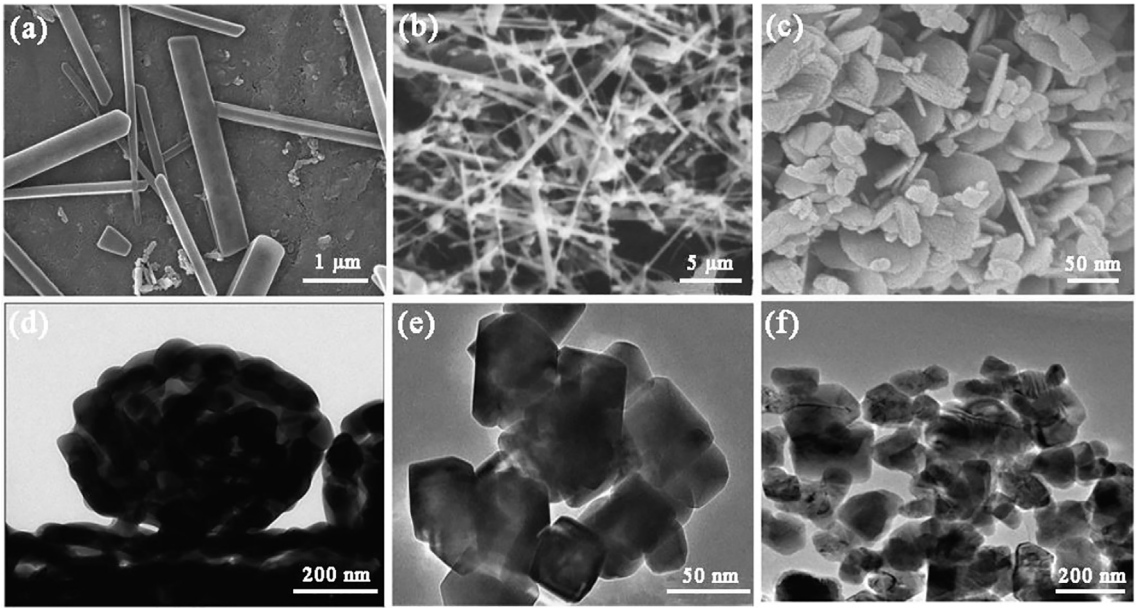

Fig. 2. Morphology of nanostructured *o*-$LiMnO_2$ with various synthesis methods (a, b) nanorods [23,24], (c) nanoplates [25], (d) nanospheres [26] and (e, f) nano-particles [27,28]. Reproduced from Refs. [23–25,27] with permission from Elsevier. Reproduced from Refs. [26,28] with permission from the American Chemical Society.

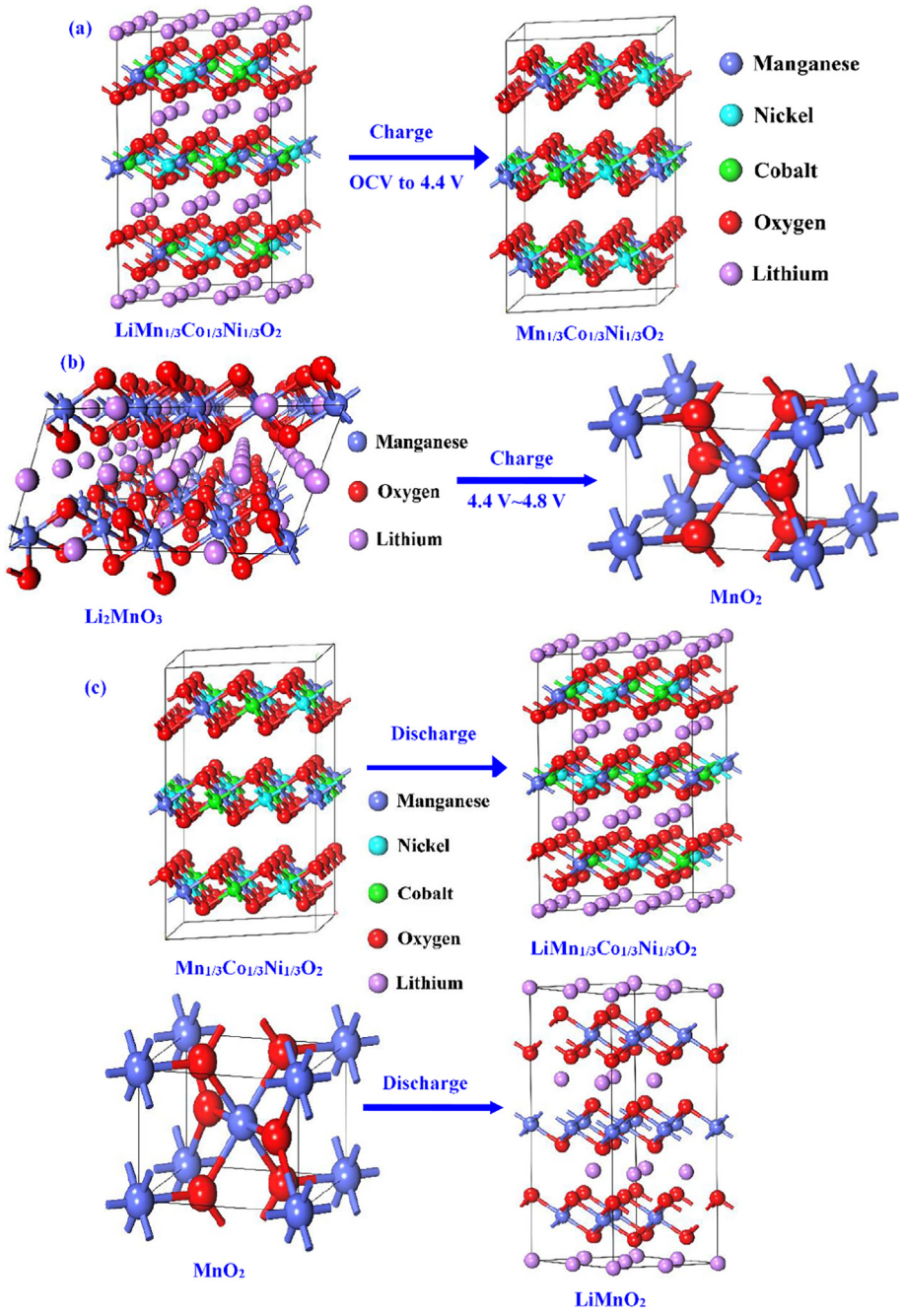

Fig. 3. Schematic diagram of structure change for $Li_2MnO_3{\cdot}LiCo_{1/3}Mn_{1/3}Ni_{1/3}O_2$ during the initial cycle [31]. Reproduced from Ref. [31] with permission from Elsevier.

could be activated and then consumed with a deintercalation of Li^+ ion from the host structure, and then O^{2-} vacancy appears, resulting in sectional cation disordering and formations of β-MnO_2 phase (Fig. 3b). Therefore, the charge mechanism above 4.40 V at the first cycle is as follows:

$$xLi_2MnO_3 \cdot (1-x)Co_{1/3}Mn_{1/3}Ni_{1/3}O_2 \overset{\text{Charge}}{\rightarrow} xMnO_2 \cdot (1-x)Co_{1/3}Mn_{1/3}Ni_{1/3}O_2 + xLi_2O \quad (2)$$

Obviously, the formation of Li_2O results in an irreversible capacity loss of the Li-rich cathode. During the discharge process at the first cycle, the discharge mechanism is as follows (Fig. 3c):

$$xMnO_2 \cdot (1-x)Co_{1/3}Mn_{1/3}Ni_{1/3}O_2 + Li^+ \overset{\text{Disharge}}{\rightarrow} xLiMnO_2 \cdot (1-x)Co_{1/3}LiMn_{1/3}Ni_{1/3}O_2 \quad (3)$$

In the following cycle, the charge and discharge mechanism is as follows:

$$xLiMnO_2 \cdot (1-x)Co_{1/3}LiMn_{1/3}Ni_{1/3}O_2 \underset{\text{Discharge}}{\overset{\text{Charge}}{\rightleftharpoons}} xMnO_2 \cdot (1-x)Co_{1/3}Mn_{1/3}Ni_{1/3}O_2 + Li^+ + e^- \quad (4)$$

However, during the discharge process at the first cycle, the a few Li^+ ions may enter the octahedral interstitial sites of manganese ions, and a layered $Li_{0.9}MnO_2$ can be formed step by step *via* an unordered cation arrangement. The formed $Li_{0.9}MnO_2$ can translates into spinel $LiMn_2O_4$ in following cycles, resulting in a voltage attenuation [32]. The capacity fading mechanism of Mn-based Li rich cathode can be summarized as follows: (1) The oxidation of electrolyte because of high charge voltage; (2) the formation of Li_2O at the first cycle; (3) structure transformation to

spinel phase. Hence, the nanostructure or micro-nano structures have been considered as one of an efficient strategy to improve the electrochemical performances of Mn-based Li rich materials. The nanostructure can shorten the lithium ion migration pathway, and then enhance the rate capacity even at high rates [33,34]. The micro-nano structures consisted of nanoparticles can contribute to decreasing the side reactions, and then improves cycling stability. Miao et al. [35] prepared nanosized $xLi_2MnO_3\cdot(1-x)LiNi_{1/3}Co_{1/3}Mn_{1/3}O_2$ (x = 0.2, 0.4, 0.6, 0.8) by microwave hydrothermal method. The particle size is of 50–100 nm. The $0.4Li_2MnO_3\cdot0.6LiNi_{1/3}Co_{1/3}Mn_{1/3}O_2$ shows the best cycling performance, and it exhibits an initial specific capacity of 325 mAh g^{-1} with a capacity retention of about 72.2% at 0.1C after 50 cycles.

The one-dimensional (1D) structures can offer a shortened diffusion path of ions and electrons along the narrow radial dimensions. Especially, 1D porous structures consisted of nanoparticles are attractive because the connected porous framework can not only allow for effective active mass-electrolyte contact but also alleviate the strains related to the structure transition upon repeated lithium ion insertion [36]. Kim's group [37] fabricated Li $[Ni_{0.25}Li_{0.15}Mn_{0.6}]O_2$ nanowires with diameter of 30 nm via template-free synthesis. The nanowires show an improved initial specific capacity of 311 mAh g^{-1} at 0.3C because of the decreased Li-ion diffusion distance and stabilizing structure with Ni^{2+} as pillars. Hosono and partners [38] synthesized $Li_{1.2}Mn_{0.533}Ni_{0.133}Co_{0.133}O_2$ hollow nanowires by electrospinning. After heating, the hollow structure is clear. It shows an initial discharge capacity of over 250 mAh g^{-1} at 0.1 A g^{-1}, and maintains over 200 mAh g^{-1} after 20 cycles. Lee et al. [39] synthesized $Li_{1.06}Co_{0.33}Mn_{0.49}O_2$ nanowires with a diameter of 50 nm through hydrothermal process using $Co_{0.4}Mn_{0.6}O_2$ nanowires and lithium nitrate as precursors (Fig. 4a). It shows a good rate capability, and it also indicates a high discharge capacity of 220 mAh g^{-1} even at 15C discharge rate (Fig. 4g). In addition, it also indicates a good cycle stability with a capacity retention of 92% at 1C rate after 50 cycles (Fig. 4g). Yang et al. [40] synthesized the porous $Li_{1.09}Mn_{0.545}Ni_{0.364}O_2$ nanorods (LLNMO PNRs) by an impregnation process followed by a facile solid-state reaction using the Mn_2O_3 porous nanorods as precursor. The prepared LLNMO PNRs shows a highly porous morphology of nanowire composed of interconnected nanosized subunits with a diameter of ~50 nm and a length of about 5 mm (Fig. 4b and c). The nanorods obtained an initial specific capacity of 275 mA h g^{-1} at with capacity retention of ~90% 0.2C over 100 cycles. He et al. [41] designed a 3D porous $Li_{1.2}Mn_{0.56}Ni_{0.16}Co_{0.08}O_2$ (PS-LMNC) material integrated with an in situ generated surface containing carbon-based compounds prepared by a simple method (Fig. 4d). In contrast, $Li_{1.2}Mn_{0.56}Ni_{0.16}Co_{0.08}O_2$ (CP-LMNC) was also synthesized by a traditional coprecipitation process. PS-LMNC shows more excellent cycling stability than CP-LMNC at 0.5C rate (Fig. 4e), and PS-LMNC shows an excellent capacity retention rate of 98% corresponding a very small loss of 4.5 mAh g^{-1} after 100 cycles. Moreover, PS-LMNC also shows an excellent cycling stability with a capacity of 150 mAh g^{-1} and a high capacity retention rate of 95% at 2C after 500 cycles (Fig. 4e). Moreover, a small loss of energy of PS-LMNC can be found, but no voltage decay can be found during a long cycle (Fig. 4f). Fu et al. [42] synthesized hollow porous hierarchical (HPH) $Li_{1.2}Mn_{0.96}Co_{0.12}Ni_{0.12}O_2$ (LLO) with a homogeneous flower-shaped morphology composed of small interconnected nanoplates by a solvothermal process. The hierarchical flower-shaped structure has a mean size of 20 μm, which is fabricated from tens of pyramids with a length of about 10 μm (Fig. 4h). The HPH LLO shows an excellent capacity of 154 mAh g^{-1} and a good cycle performance with an ignorable capacity fading over 200 cycles even at 10C (Fig. 4i).

Jiang et al. [33] prepared hollow $Li_{1.13}Mn_{0.565}Ni_{0.304}Mn_{0.304}O_2$ microspheres via a simple in situ template-sacrificial method, as illustrated in Fig. 5(a). The hollow microspheres are formed by a nanoscale Kirkendall effect. Thus, the hollow microspheres display a high reversible capacity of 295 mAh g^{-1} after 100 cycles and obtained 125 mAh g^{-1} at 1 A g^{-1}. Even at elevated temperature, it shows much enhanced electrochemical performance. Yang et al. [43] synthesized $xLi_2MnO_3\cdot(1-x)LiNi_{1/3}Co_{1/3}Mn_{1/3}O_2$ (x = 0.57, 0.48, and 0.44) nanoplates with a diameter of 200 nm and thickness of 60 nm through solid-state method using MnO_2 as self-template. The nanoplates with x = 0.44 obtained the highest specific capacity of 270 mAh g^{-1} among all samples.

In general, this hierarchical porous structure can provide low energy barrier for lithium ion migration, and large specific surface area accessible to the electrolyte, all of which promote the electrochemical reaction in the Mn-based cathode. In addition, the presence of a big internal cavity and a highly porous shell can accelerate the electrolyte diffusion into the internal space of the material as well as offer abundant open channels for rapid lithium ion transfer and more extra active sites for the storage of lithium ion. In addition, other strategies also have been used to enhance the rate performance and cycle stability, which mainly includes doping and surface coating. In general, there are four ways to dope the Mn-based Li-rich material: (1) Na [44], Mg [45] doped at Li site; (2) cations doped at the transition metal (TM) site, such as Cu [46], Zn [47], Cr [48], Mg[49], Al [50], La [51], Fe [52], Ti [53], Zr [54], Ru [55], Si [56], Sn [57], V [58]; (3) O substituted by F [59]; (4) B and other elements doped in the TM layer to form polyanion $(BO_4)^{5-}$ [60]. The purpose of the doping is to improve the electronic conductivity or broaden the migration channels of lithium ions. For example, Yi et al. [49] synthesized Co-free Mn-based Li-rich materials ($Li_{1.17}Ni_{0.25-x}Mn_{0.58}Mg_xO_2$) via a coprecipitation process. They used DFT + U method to prove that the doped Mg^{2+} occupy either in the Li (3a) sites or in the Ni (3b) sites of $LiMO_2$ phase for the first time, which contributed significantly to the rational design and construction high-performance Li-rich materials and the understanding of the electrochemical reaction mechanism of Li-rich materials. $Li_{1.17}Ni_{0.23}Mn_{0.58}Mg_{0.02}O_2$ shows the highest reversible capacity of about 148 mAh g^{-1} and cycle performance with a capacity retention of ~95% at 2C charge/discharge rate after 100 cycles. Ding et al. [56] synthesized Si/Sn-doped $Li_{1.2}Mn_{0.54}Ni_{0.13}Co_{0.13}X_{0.03}O_2$ (X = Si, Sn) cathodes by a sol–gel route, and Sn-doped cathode shows the highest rate capacity, especially in high discharge rates (Fig. 5b). In order to explain the reasons, Fig. 5(c–f) shows that TMO_2 (slab thickness) and Li (interslab spacing) layers are rearranged due to the Si/Sn substitution. The large radius of Sn^{4+} cations leads to the increase of TM–O–TM bond angle between two adjacent TMO_6 polyhedrons along the a/b directions and the expansion of lattice parameter a. Furthermore, the shrinkage of the slab thickness (TMO_2 layer) also causes the expansion of the Li layer spacing, which improves the rate capability of the doped materials, despite the changes of the slab thickness and interslab space exhibit an opposite trend.

Surface coating is another effective way because it can avoid the direct contact between cathodes and electrolyte, and then reduces the side reactions. The perfect coating layer should effectively restrain side reactions by serving as a physical protective barrier to reduce the direct contact between Li rich cathodes and electrolyte, and then restrains the dissolution of TM, evolution of O_2 and irreversible phase transition [61,62]. In addition, the coating layer should have high ionic conductivity, excellent electronic conductivity, good chemical stability and provide a stabilized the interface between cathode and electrolyte. In general, there are five ways to coat the Mn-based Li-rich material: (1) Carbon coating with different carbon sources [63,64] and conducting polymer

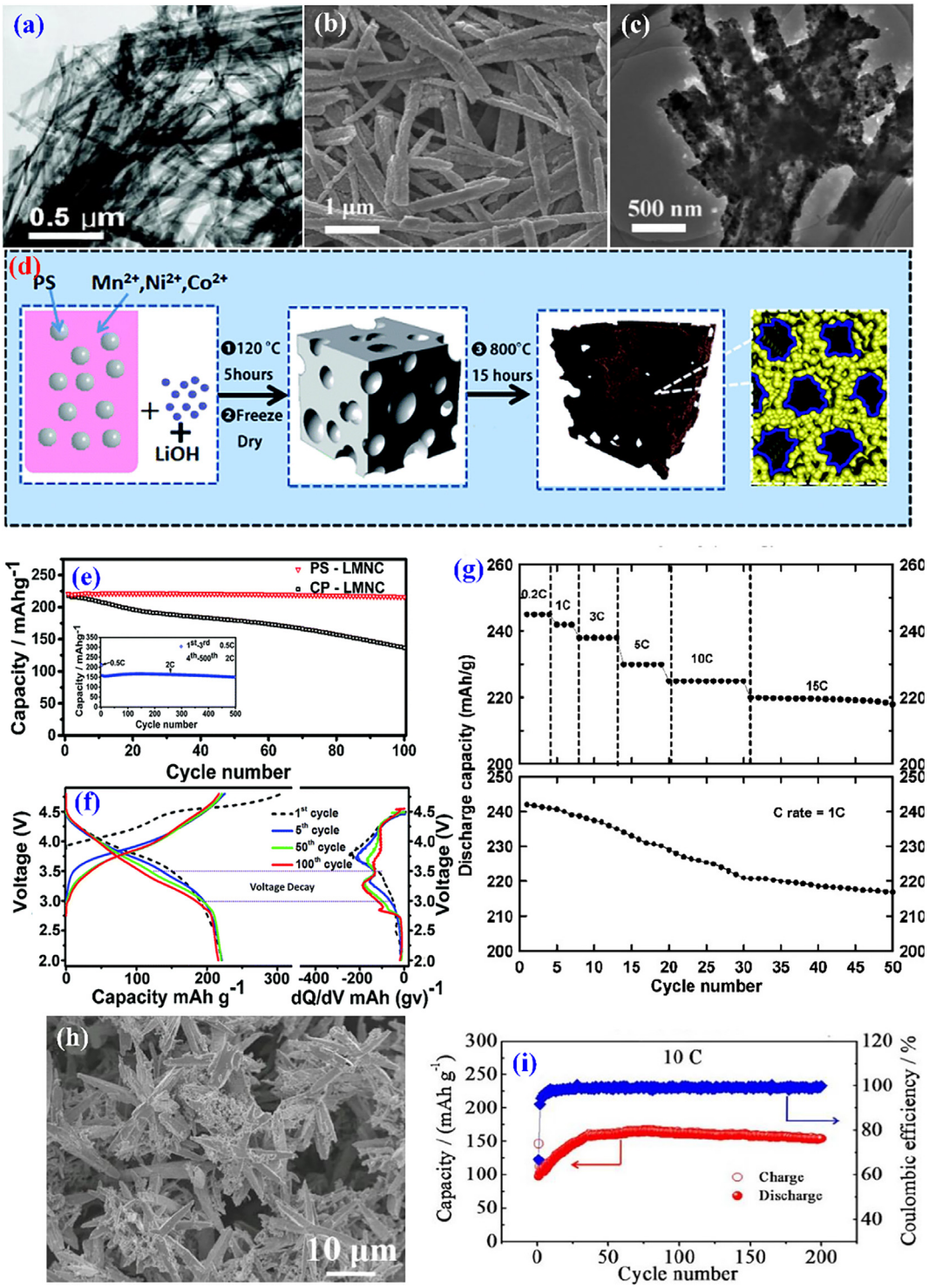

Fig. 4. (a) TEM picture of $Li_{1.06}Co_{0.33}Mn_{0.49}O_2$ nanowires [39]; (b) SEM and (c) TEM pictures of porous $Li_{1.09}Mn_{0.545}Ni_{0.364}O_2$ nanorods [40]; (d) schematic diagram of the formation of porous $Li_{1.2}Mn_{0.56}Ni_{0.16}Co_{0.08}O_2$, (e) cycle performance of CP-LMNC and PS-LMNC at 0.5C (Inset is the cycle performance of PS-LMNC at 2C), and (f) d*Q*/d*V* profiles of the PS-LMNC in the different cycles at 0.5C [41]; (g) rate performance and cycling stability of $Li_{1.06}Co_{0.33}Mn_{0.49}O_2$ nanowires [39]; (h) SEM image and (i) cycling performance of hollow porous hierarchical $0.5Li_2MnO_3{\cdot}0.5LiMn_{0.4}Co_{0.3}Ni_{0.3}O_2$ [42]. Reproduced from Refs. [39,42] with permission from the American Chemical Society. Reproduced from Refs. [40,41] with permission from The Royal Society of Chemistry.

[65,66]; (2) transition metal oxides coating, such as ZrO_2, TiO_2, Al_2O_3, MgO; (3) metal fluoride coating [59]; (4) phosphate coating [60], (5) fast ion conductors modification. For example, Xia et al. [64] reported an improved electrochemical performance of heterostructured L@S@C ($Li_{1.142}Mn_{0.475}Ni_{0.192}Co_{0.192}O_2$@spinel@-carbon) synthesized by carbonization-reduction method, and the thickness of the carbon layer is about 6 nm (Fig. 6a). The apparent shell of spinel and carbon with high electronic conductivity reduce the direct contact between Li rich cathodes and electrolyte (Fig. 6b), and L@S@C shows more excellent reversible capacity than pristine Li rich cathode at high current densities. As given in Fig. 6 (c), L@S@C delivers a discharge capacity of ~120 mAh g^{-1}, but the

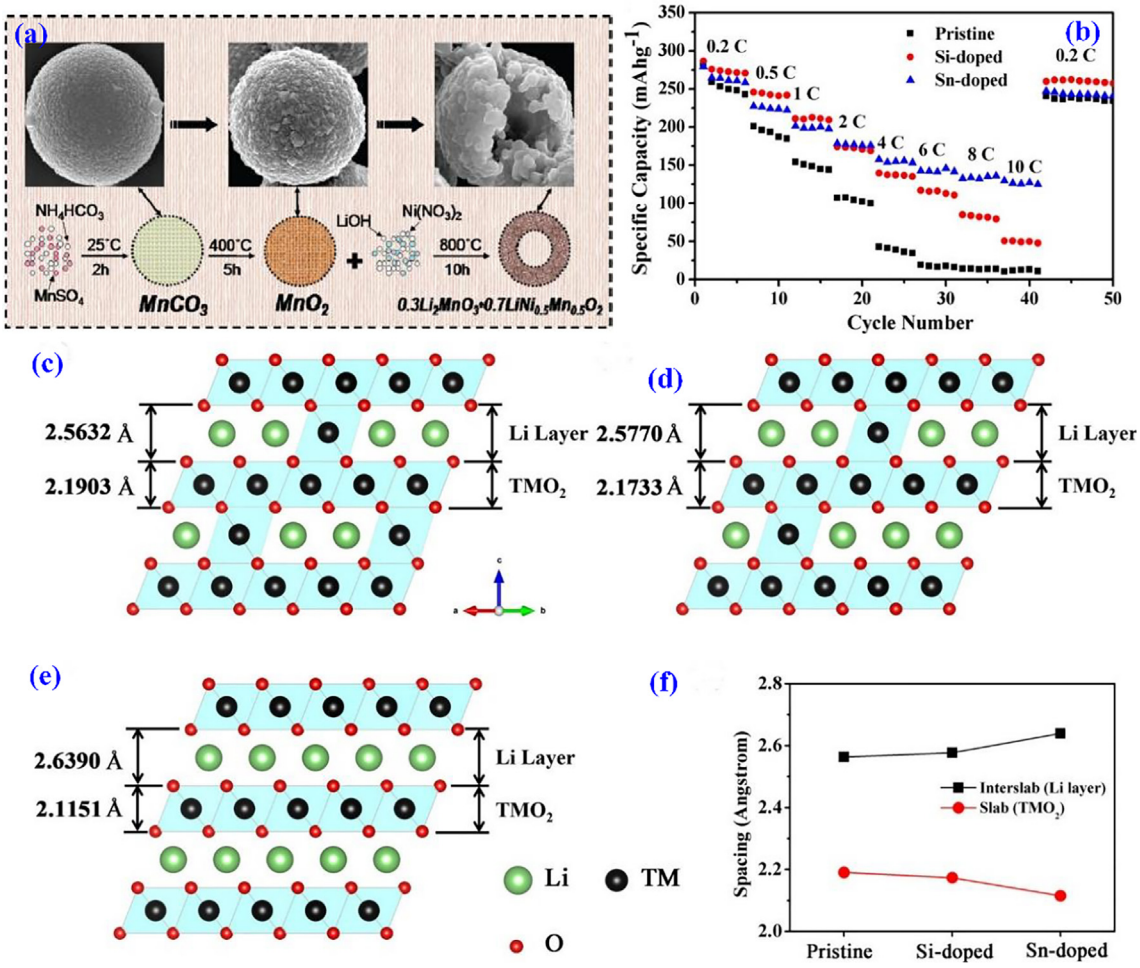

Fig. 5. (a) Schematic illustration for the synthesis of $Li_{1.13}Mn_{0.565}Ni_{0.304}Mn_{0.304}O_2$ hollow microspheres [33], (b) rate capability of $Li_{1.2}Mn_{0.54}Ni_{0.13}Co_{0.13}X_{0.03}O_2$ (X = Si, Sn) cathodes and crystal structure transformations of (c) $Li_{1.2}Mn_{0.54}Ni_{0.13}Co_{0.13}O_2$, (d) $Li_{1.2}Mn_{0.54}Ni_{0.13}Co_{0.13}Si_{0.03}O_2$, (e) $Li_{1.2}Mn_{0.54}Ni_{0.13}Co_{0.13}Sn_{0.03}O_2$ and (f) change of interslab (Li layer) and slab spacing (TMO_2) variation of $Li_{1.2}Mn_{0.54}Ni_{0.13}Co_{0.13}X_{0.03}O_2$ (X = Si, Sn) cathodes [56]. Reproduced from Ref. [33] with permission from The Royal Society of Chemistry. Reproduced from Ref. [56] with permission from the American Chemical Society.

pristine Li rich cathode almost cannot deliver capacity. The improved capacity is from the enhanced electronic conductivity because the coated conductive carbon layer can effectively decrease the polarization during cycling. Wu et al. [66] used poly (3,4-ethylenedioxythiophene) (PEDOT) and poly(styrenesulfonate) (PSS) to coat Li rich cathode ($Li_{1.2}Ni_{0.2}Mn_{0.6}O_2$), and obtained an obviously improved reversible capacity. According to the contents of 1 wt%, 3 wt% and 5 wt% PEDOT:PSS, the samples are denoted as PP1, PP3 and PP5, respectively. As shown in Fig. 6(d), the conducting polymer coated Li rich cathodes indicate higher specific capacities and more excellent cycling stability than pristine one at 1C rate, and PP3 indicates the largest reversible capacity with 146.9 mAh g^{-1} after 100 cycles among all samples [66]. The conductive polymer coating enhances the conductivity of Li rich material, and then enhance the cycle performance and reversible capacity, especially in high discharge rates.

TMOs or metal fluorides, such as MoO_x [67], Pr_6O_{11} [68], Al_2O_3 [69], Er_2O_3 [70], SnO_2 [71], FeO_x [72], CeO_2 [73], ZnO [74], TiO_2 [75], Sm_2O_3 [76], ZrO_2 [77], La_2O_3 [78], CaF_2 [79], MgF_2 [80], FeF_3 [81], CeF_3 [82] and AlF_3 [83], have been applied to coat Li rich materials. The above-mentioned coating materials may protect Li rich cathode materials from attacking by HF, and decrease the dissolution of transition metal ion, then stabilize crystal structures during cycling. For instance, Hu et al. [73] reported the preparation and electrochemical property of CeO_2 coated $Li_{1.2}Mn_{0.54}Ni_{0.13}Co_{0.13}O_2$ (COLR) by sol–gel route. As shown in Fig. 6(e), COLR shows higher reversible capacity and capacity retention of 80.4% than pristine $Li_{1.2}Mn_{0.54}Ni_{0.13}Co_{0.13}O_2$ (57.3%) after 150 cycles at 1C rate. The electrochemical performances are enhanced mainly because of the coated CeO_2 protective layer, which can restrain the cathode materials from attacking by HF, and reduce the dissolution of transition metal ion during cycling (Fig. 6f). Zheng et al. [83] used AlF_3-coating to enhance the electrochemical property of $Li_{1.2}Ni_{0.15}Co_{0.1}Mn_{0.55}O_2$ (LMR). As shown in Fig. 7(a), the pristine LMR shows a rapid capacity fade, and only delivers a capacity of 169 mAh g^{-1} with a capacity retention of about 81% after 100 cycles at 0.3C, but there is almost no capacity attenuation for the AlF_3-coated LMR. The AlF_3-coating restrains a SEI film growing process of continually creating on the surface of particle, and protects the LMR cathode from serious corrosion by HF from the electrolyte (Fig. 7b).

Metal phosphates as coated materials, such as Li_3PO_4 [84,85], $FePO_4$ [86], $AlPO_4$ [87,88], $PrPO_4$ [89], $SmPO_4$ [90], have been also applied to enhance the electrochemical property of Li rich cathode because the high electronegativity of $(PO_4)^{3-}$ polyanions can result in high reaction resistance between the coated cathode and electrolyte. Hence, metal phosphates-coated Li rich cathode usually shows excellent cycling stability. For example, Wu et al. [87] used $AlPO_4$ as coated layer to improve the electrochemical performance of $Li_{1.2}Fe_{0.1}Ni_{0.15}Mn_{0.55}O_2$. As shown in Fig. 7(c), the $AlPO_4$ (5 wt%)-

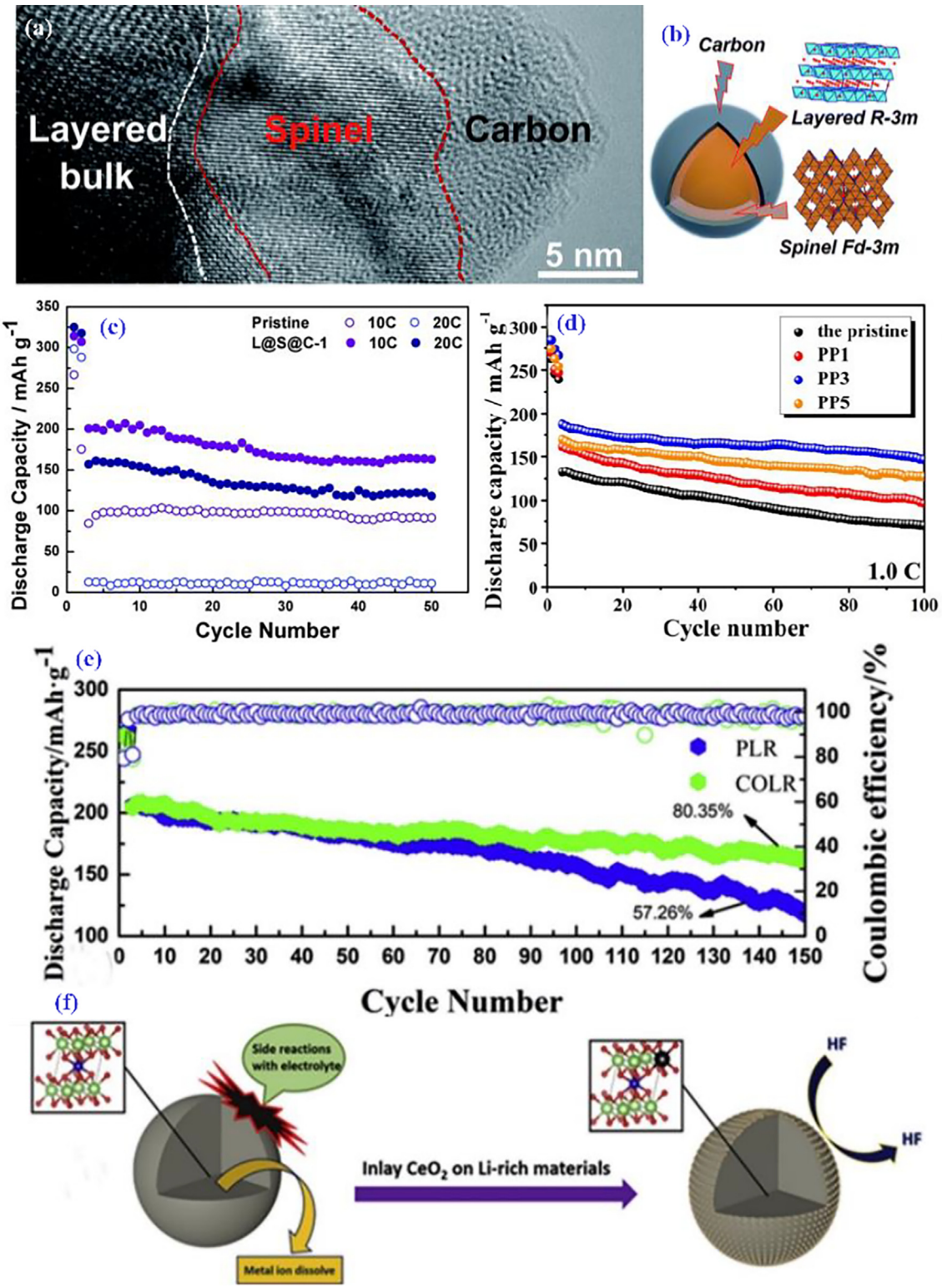

Fig. 6. (a) HRTEM image and (b) schematic diagram of L@S@C, (c) cycling stability of L@S@C and $Li_{1.142}Mn_{0.475}Ni_{0.192}Co_{0.192}O_2$ [64]; (d) cycling stability of PEDOT and PSS coated $Li_{1.2}Ni_{0.2}Mn_{0.6}O_2$ [66]; (e) cycling stability of COLR and $Li_{1.2}Mn_{0.54}Ni_{0.13}Co_{0.13}O_2$ and (f) schematic diagram of the mechanism of performance improvement by CeO_2 coating [73]. Reproduced from Ref. [64] with permission from The Royal Society of Chemistry. Reproduced from Ref. [66] with permission from the American Chemical Society. Reproduced from Ref. [73] with permission from Elsevier.

coated $Li_{1.2}Fe_{0.1}Ni_{0.15}Mn_{0.55}O_2$ shows the largest discharge capacities and best cycling stability among all samples, which shows reversible capacities of 175, 172, 137 and 120 mAh g^{-1} at 1, 2, 5 and 10C rate after 100 cycles, respectively. The $AlPO_4$-coating restrains side reaction between electrode and electrolyte, maintains more oxygen vacancy and protects the cathode from serious attack by HF from the electrolyte (Fig. 7c). In addition, the formed Li_3PO_4 phase has the characteristics of fast lithium-ion conductor,

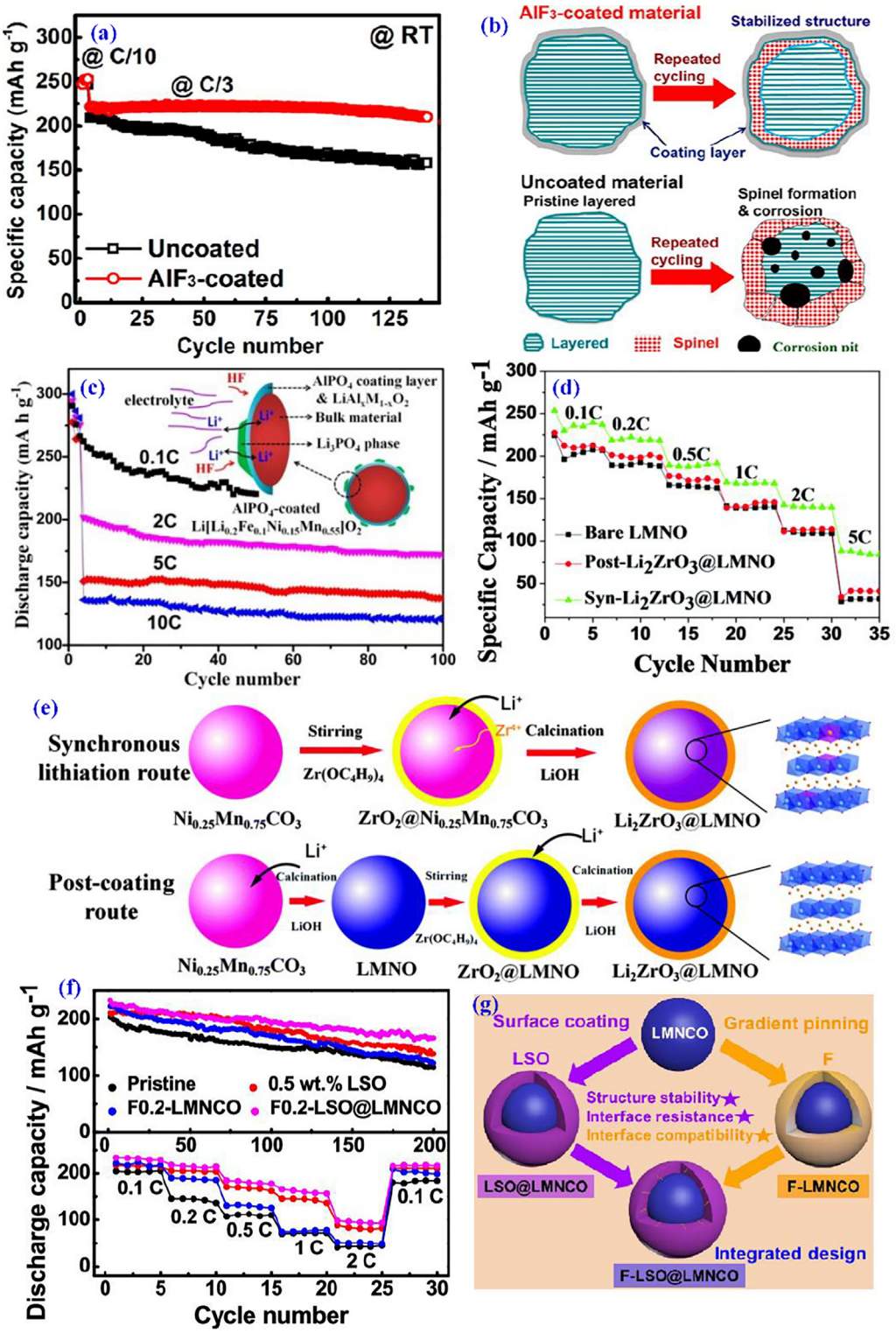

Fig. 7. (a) Cycling stability of pristine and AlF_3-coated $Li_{1.2}Ni_{0.15}Co_{0.1}Mn_{0.55}O_2$, (b) mechanism of electrochemical performance improvement after AlF_3-coating [83]; (c) cycling stability of $AlPO_4$-coated $Li_{1.2}Fe_{0.1}Ni_{0.15}Mn_{0.55}O_2$ at different rates (Inset is the mechanism of electrochemical performance improvement after $AlPO_4$-coating) [87]; (d) rate capability and (e) schematic diagram of the synthesis process of pristine and Li_2ZrO_3-coated $Li_{1.2}Mn_{0.6}Ni_{0.2}O_2$ with different synthesis processes [93]; (f) cycling performance and rate capability of pristine and modified LMNCO, (g) schematic illustration of integrated surface design for F-doped Li_2SnO_3-coated LMNCO [95]. Reproduced from Refs. [83,87,95] with permission from the American Chemical Society. Reproduced from Ref. [93] with permission from The Royal Society of Chemistry.

and then improve the transfer ability of lithium ion during cycling. Hence, $AlPO_4$-coated $Li_{1.2}Fe_{0.1}Ni_{0.15}Mn_{0.55}O_2$ shows excellent reversible capacity and cycling stability.

A perfect coating material should have such features: (1) Serving as a protective layer between electrolyte and cathode, (2) possessing excellent electronic/ionic conductivity inherently, (3) high chemical stability. Hence, some Li-ion conductors, such as Li_2SnO_3 [91], Li_2ZrO_3 [92,93] and Li_2SiO_3 [94], have been used as a coating film to enhance the lithium-ion conduction at Li rich cathode/ electrolyte interface, and then improve the electrochemical perfor-

mance. Zhang et al. [93] synthesized Li_2ZrO_3-coated $Li_{1.2}Mn_{0.6}Ni_{0.2}O_2$ materials by synchronous lithiation coating process and post-coating route (Fig. 7e), which are denoted as syn-LZO@LMNO and post-LZO@LMNO, respectively. The synchronous lithiation coating process merely needs one-step crystallization heat treatment, which benefits large-scale production and the formation of integrated coating layer (Fig. 7e). The syn-LZO@LMNO shows more excellent rate capability and higher discharge capacity than pristine and post-LZO@LMNO (Fig. 7d). The Li_2ZrO_3-coating restrains dissolution metal ions and side reaction between Li rich cathode and electrolyte, and improves the ionic conductivity. Li_2SnO_3 with 3D lithium ion diffusion channel has a similar structure with monoclinic Li_2MnO_3, which can form well-matched interface between Li_2SnO_3 and Li_2MnO_3-based Li rich cathode. To further stabilize the interface between Li rich cathode and electrolyte, F-doped Li_2SnO_3 was used to modify Li-rich cathode [95]. Wang et al. [95] synthesized pristine $Li_{1.2}Mn_{0.56}Ni_{0.17}Co_{0.07}O_2$(LMNCO), F-doped $Li_{1.2}Mn_{0.56}Ni_{0.17}Co_{0.07}O_{1.98}F_{0.2}$ (F0.2-LMNCO), Li_2SnO_3 (0.5 wt%) coated LMNCO (LSO@LMNCO) and $Li_2SnO_{2.98}F_{0.2}$ (0.5 wt%) coated LMNCO (F0.2-LSO@LMNCO) by a sol–gel route. The result shows that F-doped LSO coated Li rich cathode shows the largest discharge capacity and the most excellent cycling stability, and the capacity is 1.2, 1.4, and 1.5 times LSO@LMNCO, F0.2-LMNCO and pristine one, respectively (Fig. 7f). In addition, F0.2-LSO@LMNCO also shows the most excellent rate capability among all samples (Fig. 7f). The electrochemical properties are enhanced mainly because of the coated F-doped Li_2SnO_3 protective layer, which can protect the cathode materials from attacking by HF, and improves the structural stability (Fig. 7g).

In summary, Mn-based Li-rich cathode materials have been regarded as hopeful cathode candidates for high-performance LIBs because of the high capacity and high energy density. Nonetheless, the inherent drawbacks including low initial coulombic efficiency, serious voltage attenuation and poor cycling stability limit the large-scale applications. To resolve these challenges, various strategies including morphology control, doping, surface coating, have been proposed. The hierarchical porous structure can provide low energy barrier for lithium ion migration, and large specific surface area accessible to the electrolyte, all of which promote the electrochemical reaction in the Mn-based Li rich cathode. In addition, the highly porous shell can accelerate electrolyte diffusion into the internal space of the material as well as offer abundant open channels for rapid lithium ion transfer and more extra active sites for the storage of lithium ion. The oxygen activity has been viewed as playing a crucial role in the voltage fading and capacity degeneration of Mn-based Li rich cathode. The doping is an effective strategy to decrease voltage decay by blocking of transition metal ions migration and the stabilizing the transition metal and oxygen atom layers. The doping also can reduce the cation intermixing by altering the local coordination environment and oxygen activity, and then reduce oxygen evolution and lithium loss. The surface coating can alleviate the side reaction at electrode/electrolyte interface, decrease the surface lattice oxygen evolution, and then increase retention of oxide ion vacancy in the lattice after the first charge. In addition, the solid electrolytes and ion conductive coating materials can improve the interfacial stability of Li-rich materials as compared with another coating material that owns low lithium conductivity and electrical conductivity and can block lithium migration channels. Developing multiple strategies, such as a combination of coating and doping, may be a better choice to suppress oxygen evolution and phase transition than single strategy.

Despite the high energy density and specific capacity of Li-rich cathode materials, the major challenges of Mn-based Li-rich cathodes are low initial coulombic efficiency, severely continuous voltage decay and transitional metals dissolution. These intractable challenges may strongly limit the large-scale applications of Mn-based Li-rich cathodes. Obviously, spinel Mn-based oxide ($LiMn_2O_4$) is a competitive cathode material for extensive large-scale applications of LIBs because of its outstanding advantages of excellent thermostability, guaranteed safety, low cost, environmental friendliness, relatively good power density and acceptable energy density. Hence, at the present stage, $LiMn_2O_4$-based material has served as a promising and inexpensive alternative cathode materials.

4. Nanostructured spinel $LiMn_2O_4$ cathode material

Spinel $LiMn_2O_4$ has been widely investigated as a hopeful material for LIBs because of its inherent advantages of large energy density, high output voltage, low cost, and excellent safety. Therefore, spinel $LiMn_2O_4$ may become attractive material of new-generation commercial LIBs. $LiMn_2O_4$ is a cubic spinel with *Fd-3 m* space group (Fig. 1c) [11]. The oxygen atoms form a cubic packed structure and occupy 32e sites. The Li atoms are located on the tetrahedral 8a sites, while the Mn atoms are positioned on the octahedral 16d sites. The tetrahedral 8a sites and the octahedral 16d sites form a three-dimensional pathway during the Li ion extraction process. And the empty octahedral 16c sites are conducive to lithium ions transfer from one 8a position into another 8a position. Lithium extraction can cause a plateau at about 4 V and lithium insertion occurs at about 3 V (*vs.* Li^+/Li^0), which corresponds to produce $Li_{1-x}MnO_4$ and $Li_{1+x}Mn_2O_4$, respectively. In addition, the spinel structure of $LiMn_2O_4$ is relatively stable in thermodynamics compared to layered electrode material. Nevertheless, $LiMn_2O_4$ also has some shortcomings. The practical application of spinel $LiMn_2O_4$ is limited because of capacity fade during cycling, which can be ascribed to two reasons. One reason is Mn dissolution by a disproportion reaction ($2Mn^{3+}_{(solid)} = Mn^{2+}_{(solid)} + Mn^{4+}_{(solution)}$), and then the spinel type $LiMn_2O_4$ transforms into defective spinels [26]. Another reason is the crystallographic structure conversion from cubic to tetragonal phase by Jahn-Teller distortion of high spin Mn^{3+} ions [96]. Thus, a lot of methods have been proposed to resolve these issues, such as the preparation of nanostructured materials, or by surface coating and cations doping to enhance the electrochemical property of materials.

Recently, different morphologies of the nanosized $LiMn_2O_4$ have been broadly studied to improve the cycle stability and rate capabilities. The nanostructure can drastically reduce ionic diffusion distances for Li^+ insertion/extraction, promote electronic transport and can also improve the contact area between the electrode and the electrolyte [97]. Thus, the nanostructured $LiMn_2O_4$ materials with different morphologies, such as nanoparticles [98], nanofibers [99], nanosheets [100], hollow microspheres [101], nanorods [102], nanowires [103], nanotubes [104], porous $LiMn_2O_4$ nanorods [105], hollow cubes [106], porous morphology [107], hollow nanofibers [108], mesoporous morphology [109], and microsphere with yolk structure [110], show excellent electrochemical performance. The synthesis process and electrochemical property of different morphologies are summarized in Table 2. For example, Lee [103] et al. synthesized well-dispersed ultrathin $LiMn_2O_4$ nanowire by solid-state lithiation of α-MnO_2 nanowire (Fig. 8a), which showed ultrahigh discharge capacity and high cycle performance at high current density (Fig. 8b). The $LiMn_2O_4$ cathode indicates a mean capacity of 105, 100 and 78 mAh g^{-1} at 10, 60 and 150C discharge rates when the charge rate is 1 C, respectively. The 1D nanostructures give rise to Li^+ intercalation kinetics and high structure stability for the $LiMn_2O_4$. Cheng et al. [105] prepared porous $LiMn_2O_4$ nanorods by using porous Mn_2O_3 nanorods as the self-supported template. As shown in Fig. 8(c), the as-synthesized porous $LiMn_2O_4$ nanorods display excellent rate performance and cyclic stability. The initial specific capacity reaches 105 mAh g^{-1} at

Table 2
Synthetic method and electrochemical performance of nanostructured $LiMn_2O_4$ cathode materials.

Morphology	Synthesis method	Discharge capacity (mAh g^{-1})	Capacity retention	Rate capability (mAh g^{-1})	Ref.
Porous structure	Template method	118 at 0.1A g^{-1}	93% after 10,000 cycles at 9C	108 at 5000 mA g^{-1}	[107]
nanorods	Solid-state reaction	105 at 10C	90% after 500 cycles at 10C	105 at 10C	[105]
nanotubes	Solid-state reaction	115 at 0.1C	70% after 1500 cycles at 5C	~ 80 at 10C	[104]
Ultrathin nanowires	Solvothermal reaction	125 at 0.1C	Around 105 mAh/g after 100 cycles at 10C	100 at 60C	[103]
Porous hollow nanofibers	Electrospinning technique	120 at 15 mA g^{-1}	87% after 1250 cycles at 1C	56 at 16C	[108]
Ordered mesoporous	Solid state reaction	~100 at 0.1C	94% after 500 cycles at 1C	~80 at 5C	[109]
Yolk-structured spheres	Solid-state reaction	128.9 at 0.2C	86.6% after 300 cycles at the rate of 1C at 55 °C	89.7 at 10C	[110]

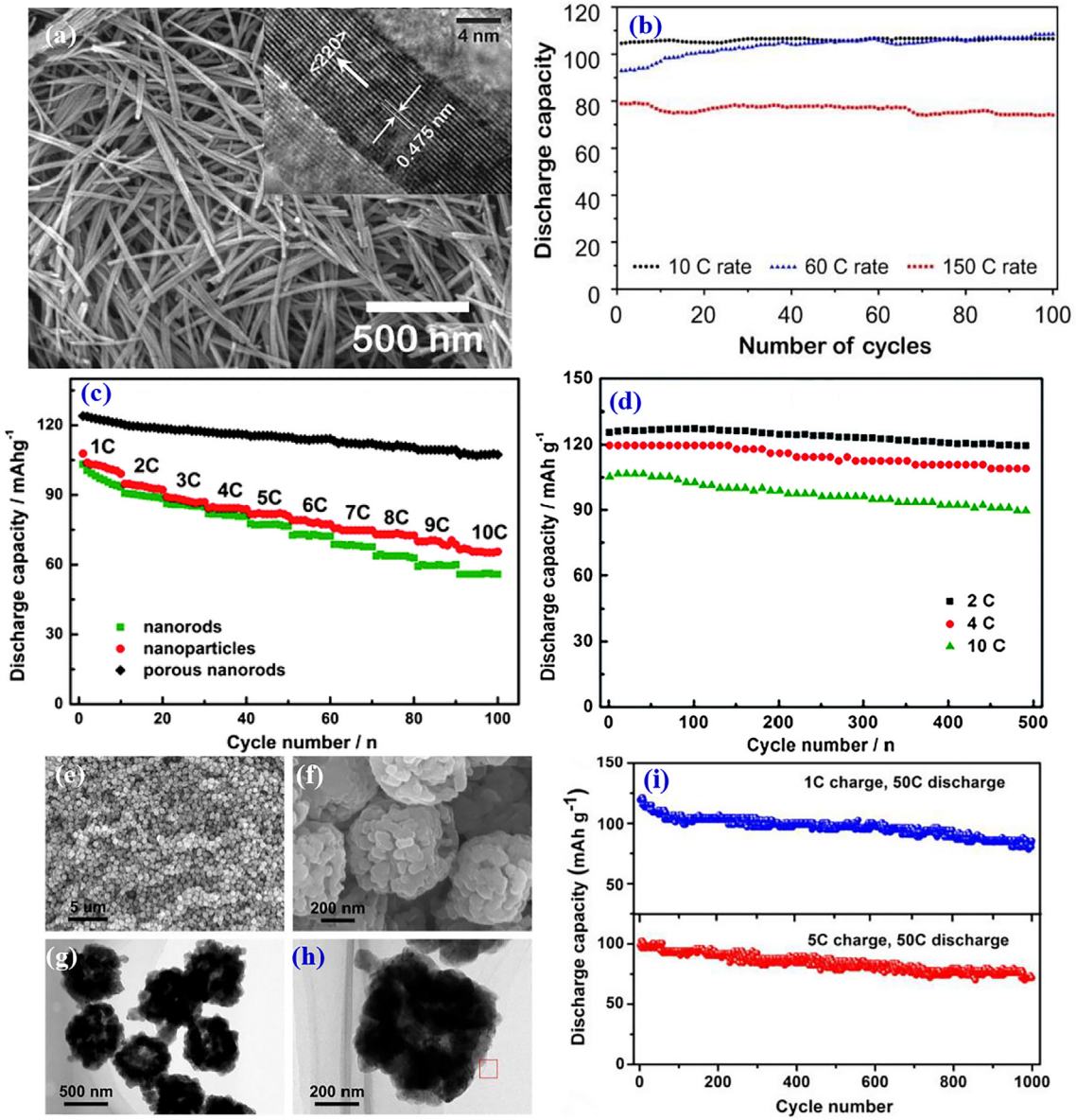

Fig. 8. (a) SEM image (Inset is HRTEM image) and cycling stability of ultrathin $LiMn_2O_4$ nanowire [103]; (c) schematic diagram of the formation for porous $LiMn_2O_4$ nanorods, (d) rate capability of $LiMn_2O_4$ with different morphologies [105]; (e, f) SEM, (g, h) TEM images and (i) cycling stability of hollow $LiMn_2O_4$ cube [106]. Reproduced from Refs. [103,106] with permission from the American Chemical Society. Reproduced from Ref. [105] with permission from The Royal Society of Chemistry.

10C rate, and the capacity retention reaches 90% after 500 cycles at this high rate. In addition, the porous $LiMn_2O_4$ nanorods show high capacities of 119, 109, and 90 mAh g^{-1} after 500 cycles at 2, 4, and 10C, respectively (Fig. 8d). This outstanding electrochemical property can be ascribed to the special porous 1D nanorods, which offers interconnected pores for electrolyte infiltration and transportation. Wu et al. [106] prepared hollow $LiMn_2O_4$ cube with exposed {111} plane by a simple coprecipitation method with a

uniform particle size of about 0.5 μm (Fig. 8e, f) and porous cube structure (Fig. 8g), which was consisted of nanoparticles with a size of ~50 nm (Fig. 8h). It shows ultrahigh discharge capacity with an initial capacity of 119 (1 C charge rate) and 96.5 mAh g^{-1} (5 C charge rate) at 50 C discharge rate, respectively, and good cycle performance with a high capacity retention rate of over 70% (Fig. 8i).

In general, the porous structure could provide direct and rapid ion transport pathways, promote the insertion/extraction of Li^+, improve the utilization efficiency of the material, and decrease the polarization. The porous structure can accelerate the permeation of electrolyte and offers internal void space to effectually accommodate the volumetric change during cycling.

Surface coating is also an efficient way to restrain dissolution manganese ions by protecting $LiMn_2O_4$ particles from the attack of HF, and enhance the electrochemical property of $LiMn_2O_4$ by coating various conductive carbon materials (amorphous carbon [111], graphene [112], graphite [113]), conducting polymer [114,115], oxides (MgO [116], Al_2O_3 [117,118], SiO_2 [119], ZrO_2 [120], TiO_2 [121], CeO_2 [122]), phosphates ($FePO_4$ [123], $AlPO_4$ [124]), fluorides (MgF_2 [125], FeF_3 [126], LaF_3 [127]), solid-state electrolyte [128] and MXene [129]. For example, Lai et al. [118] synthesized Al_2O_3-coated $LiMn_2O_4$ by using stripping and in situ self-assembly of γ-AlOOH. As shown in Fig. 9(a), the AlOOH dissolved in the water becomes a gel form, and coat on the surface of $LiMn_2O_4$ particles due to the absorption function. After a calcination, 3D hierarchical Al_2O_3 nanoplate can be coated on the surface of $LiMn_2O_4$ particles by a in situ self-assembly technology. The cycling stability of the coated $LiMn_2O_4$ at 55 °C is given Fig. 9(b), and an obvious capacity fading of all samples can be found at elevated temperature. The pristine $LiMn_2O_4$ only shows a reversible capacity of 70 mAh g^{-1} at 1C after 300 cycles, but Al_2O_3 (1 wt%)-coated $LiMn_2O_4$ shows a reversible capacity of 105 mAh g^{-1} with a high capacity retention of 93.6% after 500 cycles. The 3D Al_2O_3 layer suppresses the formation of SEI film and the dissolution of Mn at elevated temperature. Zhang et al. [128] used solid-state electrolyte coat $Li_{1.08}Mn_{1.92}O_4$, and prepared xLiNbO$_3$–(1–x/2) $Li_{1.08}Mn_{1.92}O_4$ cathodes by a solid-state reaction. The thickness of $LiNbO_3$ is about 5–8 nm (Fig. 9c). The uncoated $Li_{1.08}Mn_{1.92}O_4$ shows a reversible capacity of 103 mAh g^{-1} with a capacity retention of 76.3%, but 0.06LiNbO$_3$–0.97$Li_{1.08}Mn_{1.92}O_4$ shows a reversible capacity of 111 mAh g^{-1} with a capacity retention of 85.7% at 0.5C after 100 cycles (Fig. 9d). The dissolution of Mn can be effectively restrained by the coated $LiNbO_3$ film, which retains an excellent ionic conductivity between $Li_{1.08}Mn_{1.92}O_4$ and electrolyte. The $Ti_3C_2T_x$ (MXene) can be also used as coating layer to enhance the electrochemical property of electrode materials for Li-ion batteries because it possesses high electronic conductivity (3500–5700 S cm^{-1}), low lithium-ion diffusion barrier (0.07 eV) and outstanding mechanical property [130,131]. Wei et al. [129] prepared crumpled $Ti_3C_2T_x$ nanosheet encapsulated $LiMn_2O_4$ (LMOCT) and $LiMn_2O_4$/$Ti_3C_2T_x$ (LMOT) by an electrostatic self-assembly route (Fig. 9e). LMOCT shows more excellent rate capability and cycling stability than LMOT and LMO (Fig. 9f, g) at elevated temperature, and the capacity losses of LMOCT, LMOT and LMO are 18.4%, 18.7% and 36.7% at 2C rate after 200 cycles, respectively.

In general, the ideal coating material for $LiMn_2O_4$ need have the following characteristics: (1) The coating material should have remarkable electronic/ionic conductivity; (2) the preparation process of coated $LiMn_2O_4$ should be easy and cheap; (3) the coating material should have high chemical stability in HF, and also can protect $LiMn_2O_4$ powder from the attack of HF; (4) the coating material should have excellent mechanical property to prevent the appearance of cracks during cycling.

$LiMn_2O_4$ belongs to Fd-3 m space group, and manganese ions ($3d^3$, $3d^4$) occupy 16d site of octahedron, which is easily replaced by lithium ions (2 s^0) to form lithium manganese oxides with non-stoichiometric ratio, without causing structural changes. Therefore, the substitution of a small amount manganese ions by other metal ions does not cause structure change of $LiMn_2O_4$. Hence, the substitution of manganese ions by other metal ions can fully inhibit the occurrence of Jahn-Teller effect, and effectively improve the cycle life and restrain the capacity fading. The doping of $LiMn_2O_4$ materials are mainly divided into four types:

(1) It only increases the average valence state of Mn, and inhibits the Jahn-Teller effect. The mainly doped metal ions include Mg^{2+} [132–134], Zn^{2+} [135,136], Al^{3+} [137–139], Sc^{3+} [140], Ga^{3+} [141,142], Cu^{2+} [143]. A small amount of doping of these ions can enhance the cycling property and high temperature performance of LIBs. For example, Myung et al. [139] found that Al doping can suppress the volume change of $LiMn_2O_4$ because Al–O bonding is much stronger than that of Mn–O. The $LiAl_{0.3}Mn_{1.7}O_4$ shows a lower discharge capacity than pristine one, but the former shows higher cycling stability than pristine one at elevated temperature.

(2) It not only increases the average valence state of Mn but also enhances the stability of spinel structure. These ions mainly include Cr^{3+} [144–146], Co^{3+} [147–149] and Ni^{2+} [150–152]. The radius of these ions is not different from that of Mn ion, and their M–O bond energy is generally larger than that of Mn–O bond energy, which strengthens the crystal structure and inhibits the expansion and contraction of crystal cells. Therefore, the spinel structure is basically unchanged even the doping amount is large. For example, Wei et al. [152] synthesized $LiMn_{1.87}Ni_{0.13}O_4$ by a co-precipitation process. The pristine $LiMn_2O_4$ indicates an initial specific capacity of 119.7 mAh g^{-1}, and the capacity loss reaches 42.2% at 0.5C at 55 °C after 200 cycles. $LiMn_{1.87}Ni_{0.13}O_4$ shows a low initial specific capacity of 108.2 mAh g^{-1}, but the capacity loss is only 9.8%.

(3) Using rare earth (RE) elements to dope $LiMn_2O_4$ at Mn site or Na doping at Li site because the big ionic radius can broaden the lithium ion migration channel, such as La^{3+} [153–155], Ce^{4+} [153,156,157], Y^{3+} [158,159], Pr^{3+} [155], Nd^{3+} [153,160], Tb^{3+} [161], Sm^{3+} [162], Er^{3+} [162]. Moreover, RE–O has higher bonding energy than that of Mn–O at octahedral sites, and then RE ion doping often can enhance the structure stability of $LiMn_2O_4$. For example, Lee et al. [161] synthesized $LiTb_xMn_{2-x}O_4$ (x = 0, 0.01, 0.02, 0.04) by a simple sol–gel method. The pristine $LiMn_2O_4$ and $LiTb_{0.01}Mn_{1.99}O_4$ show similar initial discharge capacity at 1C rate at 60 °C, but $LiTb_{0.01}Mn_{1.99}O_4$ shows a high capacity retention with 82% than that of $LiMn_2O_4$ with 62% after 50 cycles.

(4) Using halide ion to dope $LiMn_2O_4$ at O site because the Mn-X (X = halide ion) bond energy is generally larger than that of Mn-O bond energy, such as F^- [163–165], Cl^- [166] and Br^- [167]. For example, Choi et al. [164] found that $LiMn_{1.8}Li_{0.1}Ni_{0.1}O_{3.8}F_{0.2}$ showed excellent cycling stability at elevated temperatures, and the reason could be ascribed to the relatively high initial Mn valence (>3.6+) and maintenance of excellent crystallinity in the process of insertion/extraction of lithium ions. Then, they found that $LiMn_{1.8}Li_{0.1}Ni_{0.1}O_{3.8}F_{0.2}$/C full batteries exhibited higher cycling performance than $LiMn_2O_4$/C full batteries at 0.2C rate at 60 °C [165].

5. Nanostructured spinel $LiNi_{0.5}Mn_{1.5}O_4$ cathode material

As mentioned above, the capacity deterioration of $LiMn_2O_4$ is highly associated with Mn dissolution caused by Jahn-Teller distortion, which can be suppressed by appropriate cation substitution.

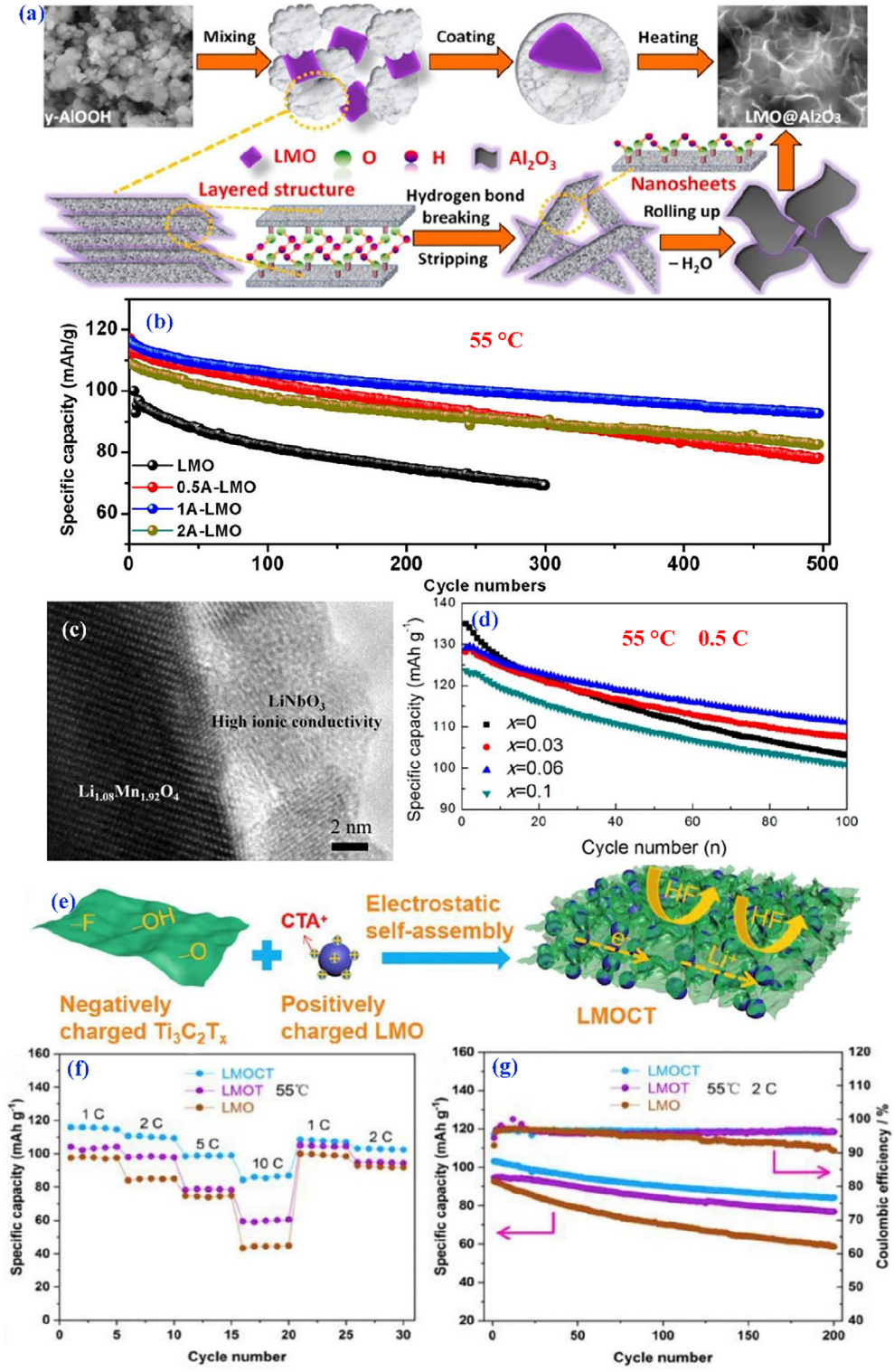

Fig. 9. (a) Schematic diagram of formation for $3DAl_2O_3$ layer coated $LiMn_2O_4$ and (b) cycling stability of pristine and Al_2O_3-coated $LiMn_2O_4$ at elevated temperature (55 °C) [118]; (c) HRTEM image of $0.06LiNbO_3$–$0.97Li_{1.08}Mn_{1.92}O_4$ cathode, (d) cycling stability of pristine and $LiNbO_3$-coated $Li_{1.08}Mn_{1.92}O_4$ at elevated temperature (55 °C) [128]; (e) Schematic diagram of synthesis of LMOCT, (f) rate performance and (g) cycle performance of pristine and coated $LiMn_2O_4$ at elevated temperature [129]. Reproduced from Refs. [118,128] with permission from the American Chemical Society. Reproduced from Ref. [129] with permission from Elsevier.

Mn ions at the 16d sites can be replaced by Ni ions. The Ni ions other than Mn in such a spinel-framework structure are exposed to an entirely different environment compared with the self-assembled lithiated metal oxide of their own kind [8]. $LiNi_{0.5}Mn_{1.5}O_4$ is a cathode material which is doped by nickel in $LiMn_2O_4$. The oxidation–reduction process of $LiNi_{0.5}Mn_{1.5}O_4$ only occurs on the Ni site, and then restrains the generation of Mn^{3+} ions and its related Jahn-Teller effect. Compared to $LiMn_2O_4$, $LiNi_{0.5}Mn_{1.5}O_4$ possesses a higher potential plateau (~4.7 V) and better cycling behavior. Because of its high voltage, $LiNi_{0.5}Mn_{1.5}O_4$ possesses a higher energy density (650 Wh kg^{-1}) than $LiMn_2O_4$ (400 Wh kg^{-1}) [168]. $LiNi_{0.5}Mn_{1.5}O_4$ has two kinds of structures, which is

ordered structure and disordered structure, respectively. One is the ordered spinel $LiNi_{0.5}Mn_{1.5}O_4$, which belongs to the face-centered spinel (Fd-3 m). The other is a simple cube ($P4_332$). The charge curve of Fd-3 m type $LiNi_{0.5}Mn_{1.5}O_4$ presents two voltage platform at 4.7 V and 4.0 V because of trace Mn^{3+}. The plateau at 4.7 V is because of the redox reaction of the Ni^{2+} to Ni^{3+} and Ni^{3+} to Ni^{4+} while the plateau at ~4 V is because of the redox reaction of the Mn^{3+} to Mn^{4+}. The theoretical capacity of $LiNi_{0.5}Mn_{1.5}O_4$ can be calculated to be 147 mAh g^{-1} when all Li-ions are extracted from $LiNi_{0.5}Mn_{1.5}O_4$. Therefore, $LiNi_{0.5}Mn_{1.5}O_4$ was regarded as one of the most promising cathode materials for LIBs [169–171]. Nonetheless, a major challenge of $LiNi_{0.5}Mn_{1.5}O_4$ is the possible corrosion reaction at the cathode/electrolyte interface at the high charge voltage, which results in a poor rate capability, especially at elevated temperatures. $LiNi_{0.5}Mn_{1.5}O_4$ can loss oxygen and generate a spinel and rock salt phase (Ni_xO or $Li_xNi_{1-x}O$ or $Li_xNi_yMn_zO$) when it is heated above 650 °C [15,171]. The high calcination temperature can result in a reduction of the manganese oxidation state from +4 to +3. $LiNi_{0.5}Mn_{1.5}O_4$ with Fd-3 m space group can be obtained by calcination above 700 °C followed by a cooling process to room temperature. $LiNi_{0.5}Mn_{1.5}O_4$ with $P4_332$ phase can be gained by using synthesis processes under oxygen or post-annealing in air below 700 °C [12,171]. In the Fd-3 m phase, Li atoms occupy the 8a site, Ni and Mn atoms discretionarily occupy the position of 16d site, O atoms occupy the 32e site in the spinel structure (Fig. 1e). For the $P4_332$ space group, Li atoms occupy the 8c position, Ni atoms occupy the 4a site, Mn atoms occupy the 12d site, O atoms occupy 8c and 24e sites, respectively (Fig. 1f) [12]. A main difference between these two crystal structures is that little Mn^{3+} ions exist in disordered $LiNi_{0.5}Mn_{1.5}O_4$ with a space groups of Fd-3 m but only Mn^{4+} ions present in the ordered $LiNi_{0.5}Mn_{1.5}O_4$ with a space group of $P4_332$. Due to the existence of Mn^{3+}, $LiNi_{0.5}Mn_{1.5}O_4$ with disordered Fd-3 m has a higher lithium-ion diffusion coefficient and higher electrical conductivity afforded by charge transfer between Ni and Mn [169].

The XRD patterns can be used to distinguish crystal structure of $LiNi_{0.5}Mn_{1.5}O_4$ with $P4_332$ and Fd-3 m space groups. As given in Fig. 10(a), the weak diffraction peaks at angle 2θ = 15°, 24°, 35°, 40°, 46°, 47°, 57° and 75° can be ascribed to $LiNi_{0.5}Mn_{1.5}O_4$ with $P4_332$ space groups, and weak diffraction peaks at 2θ = 37°, 43°, and 64° can be ascribed to $LiNi_{0.5}Mn_{1.5}O_4$ with Fd-3 m phase [170]. In addition, few rock salt phases of $Li_xNi_{1-x}O$ can be detected in $LiNi_{0.5}Mn_{1.5}O_4$ with Fd-3 m phase. In addition, form the SEAD (selected electron diffraction) patterns (Fig. 10d), it can be found that a typical spinel type diffraction pattern exists in disordered $LiNi_{0.5}Mn_{1.5}O_4$, but additional superlattice diffraction spots can be observed in ordered $LiNi_{0.5}Mn_{1.5}O_4$ [12]. Nonetheless, XRD pattern is difficult to distinguish the structure difference between $P4_332$ and Fd-3 m space groups because of the similar scattering factor of nickel and manganese. Raman or FT-IR spectroscopy was proved to be an effective way to resolve the cation ordering qualitatively. Compared with $LiMn_2O_4$, the existence of Ni(II) cation induces an increase of the number of vibration bands in the Raman spectra and FT-IR spectroscopy [171]. From Fig. 10b, more Raman peaks in the $P4_332$ structure than that of Fd-3 m one can be observed. By contrast, the FTIR spectroscopy are much less easy to distinguish the $P4_332$ and Fd-3 m structures (Fig. 10c). Two more intense peaks at about 589 and 555 cm^{-1} in $P4_332$ structure can be found, and three peaks at ~646, ~464 and ~430 cm^{-1} are missing in Fd-3 m phase. In addition, the common peak at ~624 cm^{-1} in Fd-3 m structure are stronger than at about 589 cm^{-1}, which is contrary to the $P4_332$ one.

The failure mechanism of $LiNi_{0.5}Mn_{1.5}O_4$-based batteries with $LiPF_6$-based carbonate electrolytes can be ascribed to the synergistic effect of the following possible reasons. The trace H_2O in the electrolyte can result in a generation of HF, and corresponding decomposition reactions can be summarized as follows [172–174].

$$LiF_6 + H_2O \rightarrow LiF + 2HF + POF_3 \quad (5)$$

$$POF_3 + H_2O \rightarrow PO_2F_2^- + HF \quad (6)$$

$$PO_2F_2^- + H_2O \rightarrow PO_3F^{2-} + HF \quad (7)$$

$$PO_3F^{2-} + H_2O \rightarrow PO_4^{3-} + HF \quad (8)$$

A chemical reaction between HF and $LiNi_{0.5}Mn_{1.5}O_4$ can be found,

$$16HF + 8LiNi_{0.5}Mn_{1.5}O_4 \rightarrow 12Ni_{0.25}Mn_{0.75}O_2 + NiF_2 + 3MnF_2 + 8LiF + 8H_2O \quad (9)$$

In addition, the self-discharge of the battery also leads to electrolyte decomposition and formation of HF, which promote the dissolution of $LiNi_{0.5}Mn_{1.5}O_4$. Hence, a variety of reaction products including MnF_2, LiF, NiF_2, and polymerized organic species, are observed on the $LiNi_{0.5}Mn_{1.5}O_4$ surface, which reduce the cycling stability and reversible capacity (Fig. 10e) [175].

Usually, the cycle stability and rate performance of $LiNi_{0.5}Mn_{1.5}O_4$ can be enhanced by designing novel nanostructures, which can shorten diffusion path of lithium ions and improve the contact area between electrolyte and active materials. In the past few years, various $LiNi_{0.5}Mn_{1.5}O_4$ nanostructures have been constructed, including one-dimensional (1D), two-dimensional (2D), and three-dimensional (3D) structures. Arun et al. [176] prepared $LiNi_{0.5}Mn_{1.5}O_4$ fibers consisted of nanoparticles with a diameter of ~10 nm by an electrospinning technique (Inset of Fig. 11a). The $LiNi_{0.5}Mn_{1.5}O_4$ shows an initial specific capacity of about 118 mAh g^{-1} with a high retention rate of about 93% at 150 mA g^{-1} after 50 cycles (Fig. 11a). Liu et al. [177] synthesized $LiNi_{0.5}Mn_{1.5}O_4$ hierarchical nanofibers with a diameter of 0.2–0.5 μm by an electrospinning technique, which showed a good rate performance with reversible capacities of 155, 100, 90 and 80 mAh g^{-1} at 2, 5, 10 and 15C, respectively. Cho et al. [178] synthesized uniform $LiNi_{0.5}Mn_{1.5}O_4$ nanowires through a sol–gel based template method (Fig. 11b). The average diameter of each nanowire is about 140 nm with a length of about 13 μm (Fig. 11c), which is composed of nanoparticles with a mean size of 47 nm (Fig. 11d). The $LiNi_{0.5}Mn_{1.5}O_4$ nanowire delivers a high reversible capacity of 146 mAh g^{-1}. Chen et al. [179] prepared and porous $LiNi_{0.5}Mn_{1.5}O_4$ nanorods with a diameter of 100–400 nm by a template method (Fig. 11f), which consisted of porous nanostructure (Fig. 11g). $LiNi_{0.5}Mn_{1.5}O_4$ porous nanorod shows a super cycling stability at 5 C rate, which shows a discharge capacity of 123 mAh g^{-1} during initial 300 cycles with a capacity retention of ~99%. The capacity retention also maintains 91% even after 500 cycles (Fig. 11e). The good electrochemical properties of 1D structure can be ascribed to the large surface-to-weight ratios, enhanced contact area between active materials and electrolyte, fast electrolyte infiltration, shortened transmission path along the confined radial dimension, and then can lead to fast Li ion-diffusion and low volume change during cycling. Especially, the porous 1D framework can not only allow for effective contact between $LiNi_{0.5}Mn_{1.5}O_4$ and electrolyte but also accommodate preferably the strains related to the structure change upon repeated insertion/extraction of Li ions.

Sun et al. [180] prepared porous 3D urchin-like hollow $LiNi_{0.5}Mn_{1.5}O_4$ spheres composed of nanosheets with high inner void nature and highly exposed {111} facets by template method (Fig. 11h). The as-prepared $LiNi_{0.5}Mn_{1.5}O_4$ shows super cycle performance with an excellent capacity retention rate of about 92% even at

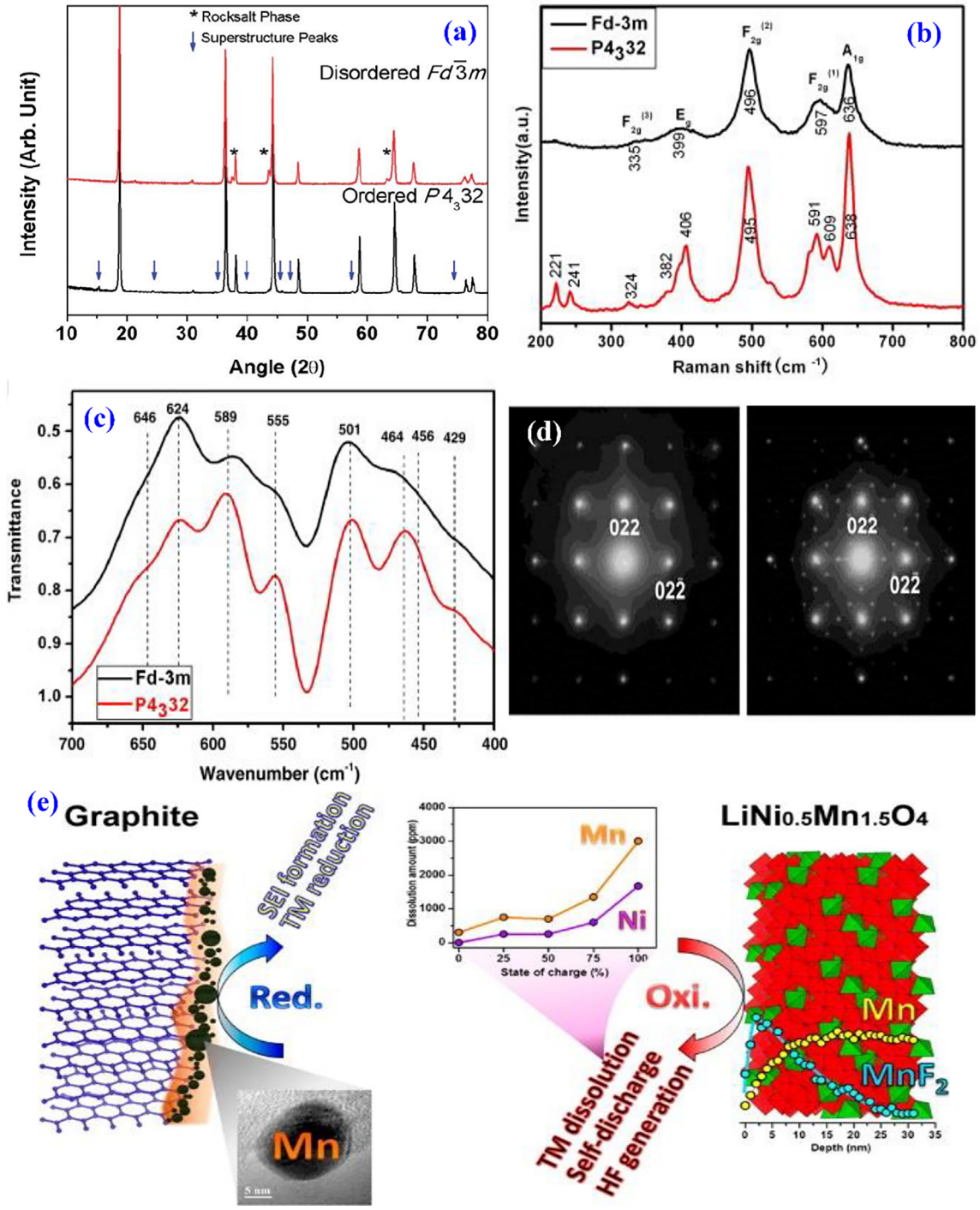

Fig. 10. (a) XRD patterns [170], (b) Raman spectroscopy [171], (c) FT-IR spectroscopy [171], (d) SEAD patterns [12] of $LiNi_{0.5}Mn_{1.5}O_4$ with Fd-3 m and $P4_332$ space groups and (e) schematic illustration of the dissolution Mn and Ni in $LiNi_{0.5}Mn_{1.5}O_4$ /graphite cell [175]. Reproduced from Refs. [12,175] with permission from the American Chemical Society. Reproduced from Ref. [170] with permission from The Royal Society of Chemistry. Reproduced from Ref. [171] with permission from Elsevier.

30 C after 1500 cycles (Fig. 11i). The void can effectively relieve the volume change in the process of insertion/extraction of Li ions (Fig. 11h). Lin et al. [181] used cubic Mn_2O_3 as templates to synthesize cubic $LiNi_{0.5}Mn_{1.5}O_4$. With increasing of calcination temperatures, the particle sizes of $LiNi_{0.5}Mn_{1.5}O_4$ increase gradually. An octahedral morphology consisted of smaller primary particles can be found at a calcination temperature of 800 °C (Fig. 11j), which possesses the predominant (111) crystal facets. The as-synthesized octahedral $LiNi_{0.5}Mn_{1.5}O_4$ shows a high cycle performance with a capacity retention of about 78% at 10C after 3,000 cycles. The exposed {111} facets promote the diffusion of Li ion, and effectively restrain the dissolution of $LiNi_{0.5}Mn_{1.5}O_4$ at high working voltage. The big secondary spherical hierarchical particle consists of smaller nano-scale or submicron primary particle. The coarse surface and the hollow structure promote the permeation of electrolyte into the electrode and thus enhance the electrochemical properties of $LiNi_{0.5}Mn_{1.5}O_4$. In general, the unique morphology can be regarded as one of promising strategy to enhance electrochemical property of $LiNi_{0.5}Mn_{1.5}O_4$, such as reversible capacity, rate performance and cycle stability.

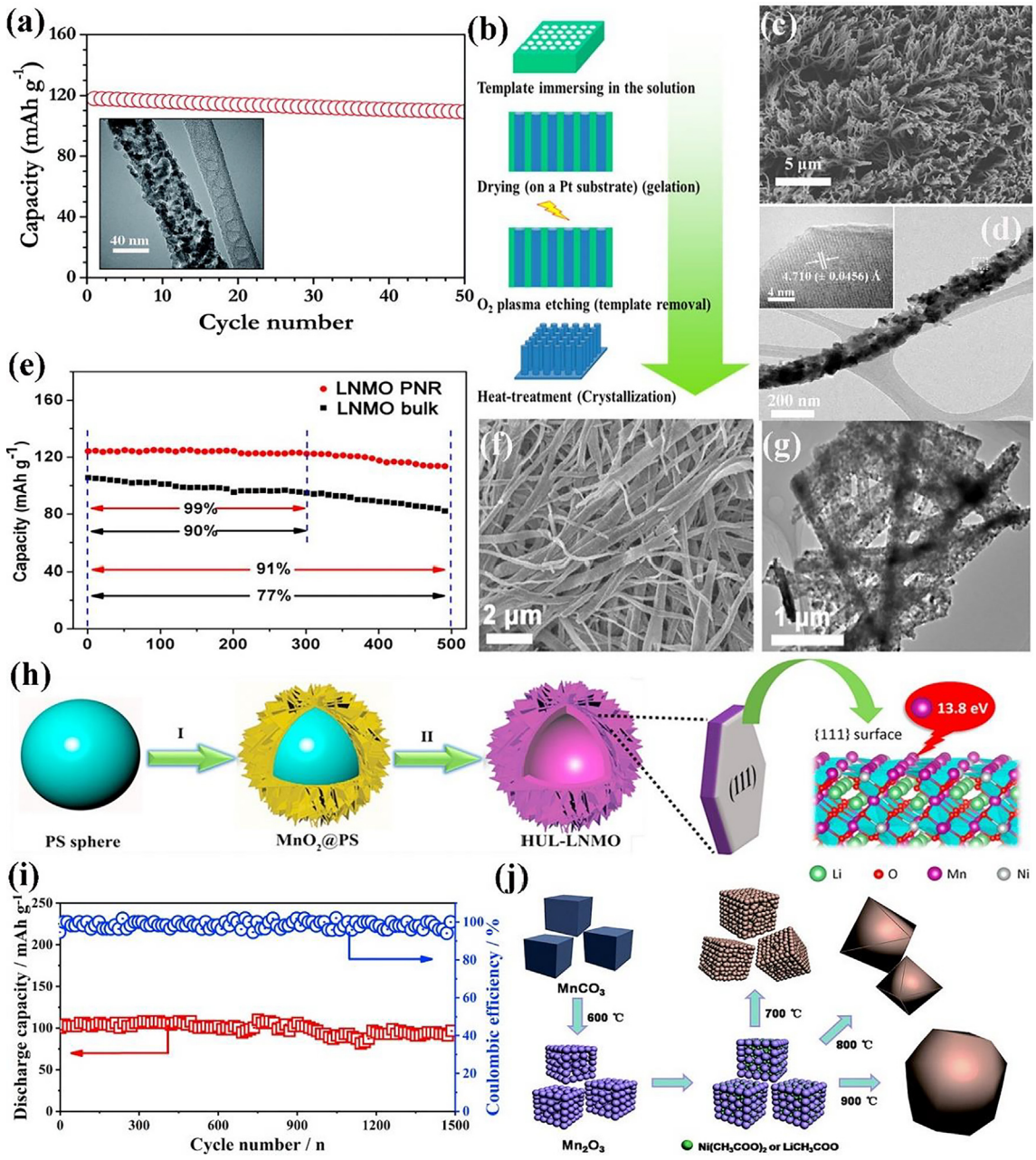

Fig. 11. (a) Cycling stability of $LiNi_{0.5}Mn_{1.5}O_4$ fibers (inset is the TEM image) [176]; (b) schematic diagram of synthesis process, (c) SEM and (d) TEM images of $LiNi_{0.5}Mn_{1.5}O_4$ nanowire [178]; (e) cycling stability of porous $LiNi_{0.5}Mn_{1.5}O_4$ nanorods and bulk one at 5C, (f) SEM and (g) TEM images of porous $LiNi_{0.5}Mn_{1.5}O_4$ nanorods [179]; (h) schematic diagram of synthesis process and (i) cycling stability of porous urchin-like hollow $LiNi_{0.5}Mn_{1.5}O_4$ spheres [180]; (j) schematic illustration of synthesis procedure of octahedral $LiNi_{0.5}Mn_{1.5}O_4$ with highly exposed (111) facet [181]. Reproduced from Refs. [176,181] with permission from The Royal Society of Chemistry. Reproduced from Refs. [178,179] with permission from the American Chemical Society. Reproduced from Ref. [180] with permission from Elsevier.

The doping was regarded as an effective strategy to enhance the electrical conductivity and lithium-ion diffusion coefficient of $LiNi_{0.5}Mn_{1.5}O_4$. The common dopants in Li^+ sites include Na^+ [182]; many dopants have been investigated in Ni^{2+} sites, including Zn^{2+} [183], Mg^{2+} [184], Cu^{2+} [185], Co^{3+} [186], Al^{3+} [187], Cr^{3+} [188,189], Fe^{3+} [190], Ga^{3+} [191], Si^{4+} [192], Ru^{4+} [193], Ti^{4+} [194], Zr^{4+} [195], Nb^{5+} [196], W^{6+} [197], Mo^{6+} [198]; the dopants in O sites include F^- [199]. Although the dopants listed above all show enhanced electrochemical properties in the $LiNi_{0.5}Mn_{1.5}O_4$, various dopants have different preferred doping positions and varying effects on the phase structure. The Na-doping in Li site often can reduce the conduction band, and then can effectively improve the electronic conductivity [200,201]. The Mg-doping can reduce polarization and enhance the electronic conductivity [202]. The Cu-doping can enhance electronic conductivity of material because of the special outer electronic arrangement of Cu(II) ion. The Zn and Al are more abundant and cheaper than most transition metals [203], and then Zn or Al doped $LiNi_{0.5}Mn_{1.5}O_4$ can be expected to be hopeful cathode material with low cost. The Ga, Co or Fe doping can enhance the electronic conductivity and structure stability [204]. The Cr doping can improve the voltage plateau and cycle performance of $LiNi_{0.5}Mn_{1.5}O_4$ because of the high oxygen affinity of Cr^{3+} ions. Especially, the $LiMn_{1.4}Cr_{0.2}Ni_{0.4}O_4$ has been has been considered as one of promising compositions due to its high potential plateau of 4.8 V and excellent cycling stability [205]. The Si doping can stabilize the disordered Fd-3 m structure, and then enhance the cycle performance and rate capability of $LiNi_{0.5}Mn_{1.5}O_4$. The Si doping can enhance the structure stability

of $LiNi_{0.5}Mn_{1.5}O_4$ because Ti–O chemical bond is stronger than Ni-O, resulting in excellent electrochemical property of Ti^{4+}-doped $LiNi_{0.5}Mn_{1.5}O_4$. The Ru doping can provide a new hopping pathway of Ni-O-Ru-O, and then promote electron transfer because of the high delocalized Ru^{4+}ions. The Nb^{5+} and Mo^{6+} doping can increase the content of active Ni^{2+} ion, and then improve reversible capacity of $LiNi_{0.5}Mn_{1.5}O_4$. For example, Yi et al. constructed Ni-rich $LiNi_{0.525}Mn_{1.425}Nb_{0.05}O_4$ [196] and $LiMn_{1.425}Ni_{0.55}Mo_{0.05}O_4$ [198] for the first time, which showed higher voltage platform, reversible capacity and cycling stability than those of pristine $LiNi_{0.5}Mn_{1.5}O_4$, resulting improving energy density. These works offer new ideas for the modulation of the component and performance of $LiNi_{0.5}Mn_{1.5}O_4$ materials and points out a research direction for the ongoing design and development of $LiNi_{0.5}Mn_{1.5}O_4$. In addition, the Nb^{5+} or Mo^{6+} doping also can improve the electronic conductivity and diffusion ability of Li ion [206–208]. The W doping can increase the length of Li–O band and reduce the distance of Ni–O and Mn–O, and then improve the diffusion ability of Li ion. The F doping can decrease Ni and Mn dissolution from HF attack, and then improve the electrochemical performance and structure stability of $LiNi_{0.5}Mn_{1.5}O_4$.

Usually, the high working voltage of $LiNi_{0.5}Mn_{1.5}O_4$ exceeds the electrochemical stability window for most organic liquid electrolytes, and then leads to serious capacity fading. A possible more effective strategy to lower or eliminate the irreversible capacity and improve cycling stability is surface coating. The surface coating can effectively avoid a direct contact between $LiNi_{0.5}Mn_{1.5}O_4$ and electrolyte by building a protective film on the surface of $LiNi_{0.5}Mn_{1.5}O_4$ particle, then restrain dissolution of metal ions and the side reactions at $LiNi_{0.5}Mn_{1.5}O_4$/electrolyte interface. Up to now, various coating materials such as carbon materials [209,210], conducting polymers [211,212], metal oxides [213–220], metal fluorides [221–223], phosphates [224–227], phosphide [228], lithium-ion conductor [229–234] and electrode materials [235,236]. Table 3 summarized the synthesis method and electrochemical property of the coated $LiNi_{0.5}Mn_{1.5}O_4$.

As a carbon-based 2D material, graphene with unique electronic property, high electronic conductivity, and large surface area has been considered as one of promising coating materials. As shown in Fig. 12(a), the coated graphene layer can promote the insertion/extraction of Li ions, restrains the attack of HF and dissolution of metal ions, and then ensure the structure stability of $LiNi_{0.5}Mn_{1.5}O_4$ during cycling [209]. Hence, the as-prepared cathode shows super cycling stability with a high discharge capacity of 91 mAh g^{-1} and excellent capacity retention of about 83% at 20C rate after 1000 cycles.

The conducting polymers possess many merits, such as excellent electronic conductivity, high chemical stability, easy synthesis, and low price. Hence, the conducting polymers have been regarded as hopeful coating materials, which can preserve the morphology of the parent material, play a role as a protective film against side reactions and HF attack, as well as to enhance electronic conductivity. Kwon et al. [211] reported a synthesis of poly(3,4-ethylenedioxythiophene) (PEDOT) coated $LiNi_{0.5}Mn_{1.5}O_4$ used cetyl trimethyl ammonium bromide (CTAB) as surfactant (Fig. 12b). The PEDOT-coated $LiNi_{0.5}Mn_{1.5}O_4$ shows good cycle performance at elevated temperatures because the PEDOT layer can effectively suppress the side reaction between the $LiNi_{0.5}Mn_{1.5}O_4$ and the electrolyte.

The oxide coatings are simple, cheap and have exhibited promising results in enhancing the electrochemical properties of $LiNi_{0.5}Mn_{1.5}O_4$ operating under various conditions. Take SiO_2 coating for example [213]. The SiO_2 coating can suppress the HF attack and the harmful side reactions between $LiNi_{0.5}Mn_{1.5}O_4$ surface and electrolyte, resulting in enhanced structure stability and cycling stability (Fig. 12c). In addition, a uniform SEI film on the surface of the SiO_2-coated $LiNi_{0.5}Mn_{1.5}O_4$ particles, which can decrease the dissolution of metal ions, and then enhance the structure stability and electrochemical performances (Fig. 12e). The SiO_2(1 wt %)-coated $LiNi_{0.5}Mn_{1.5}O_4$ indicates a high reversible capacity of about 102 mAh g^{-1} and high retention rate of about 84.4% at 40C rate after 100 cycles even at 55 °C (Fig. 12d). Moreover, the formed phase interfaces between oxides and $LiNi_{0.5}Mn_{1.5}O_4$ can offer more sites to store electrolyte and run the redox reaction (Fig. 12f) [214]. In addition, the phase interfaces can promote the reversible insertion/extraction of lithium ions, and decrease the electrochemical polarization, then enhance the cycle performance. For example, the CeO_2 (3 wt%) coated $LiNi_{0.5}Mn_{1.5}O_4$ indicates a high capacity of about 119 mAh g^{-1} with a high capacity retention of 98.3% at 1C rate after 106 cycles [214].

Compared to the metal oxides, the corresponding metal fluorides shows smaller Gibbs free energies, revealing more excellent stability. Hence, the metal fluorides are also applied to protect $LiNi_{0.5}Mn_{1.5}O_4$ materials from HF attack because of their high chemical stability in the HF environment and good thermal stability. For example, Chu et al. [221] found that the 1 wt% AlF_3 coated $LiNi_{0.5}Mn_{1.5}O_4$ indicated good cycle stability, especially at elevated

Table 3
Synthesis method and electrochemical performance of the coated $LiNi_{0.5}Mn_{1.5}O_4$.

Coating materials	Synthesis route	Optimal sample	Specific capacity (mAh g^{-1}) and capacity retention (cycle number and rate)	Ref.
Carbon	Sol-gel	C-coated (10 nm)- $LiNi_{0.5}Mn_{1.5}O_4$	125, 94% (100, 1C)	[210]
polypyrrole (PPy)	Co-precipitation	5 wt% PPy coated- $LiNi_{0.5}Mn_{1.5}O_4$	105.2, 91%(100, 1C, 55 °C)	[212]
Al_2O_3	Solid-state	0.5 wt% Al_2O_3-coated $LiNi_{0.5}Mn_{1.5}O_4$	115, 90.9%(200, 1C, 55 °C)	[215]
Co_3O_4	Solid-state	0.8 wt% Co_3O_4-coated $LiNi_{0.5}Mn_{1.5}O_4$	120, 95.8%(300, 10C)	[216]
TiO_2	Solid-state	0.9 mol% SiO_2-coated $LiNi_{0.5}Mn_{1.5}O_4$	108, 88.5%(500, 2C)	[217]
SnO_2	Sol-gel	2 wt% SnO_2-coated $LiNi_{0.5}Mn_{1.5}O_4$	103, 75%(500, 2C)	[218]
V_2O_5	Co-precipitation	5 wt% V_2O_5-coated $LiNi_{0.5}Mn_{1.5}O_4$	83.3, 85.3%(100, 2C)	[219]
$LaFeO_3$	Sol-gel	2 wt% $LaFeO_3$-coated $LiNi_{0.5}Mn_{1.5}O_4$	~130, 93.3%(100, 1C, 55 °C)	[220]
AlF_3	Sol-gel	1 wt% AlF_3 coated - $LiNi_{0.5}Mn_{1.5}O_4$	121.4, 98.1%(100, 0.2C)	[221]
YF_3	Wet chemical strategy	2.8 wt% YF_3-coated - $LiNi_{0.5}Mn_{1.5}O_4$	108, 84% (100, 0.1C)	[222]
ZrF_4	Sol-gel	2 wt% ZrF_4 coated - $LiNi_{0.5}Mn_{1.5}O_4$	117.1, 95.5%(120, 0.1C)	[223]
YPO_4	Sol-gel	3 wt% YPO_4 coated $LiNi_{0.5}Mn_{1.5}O_4$	~106, 77.5%(240, 0.1C)	[226]
ZrP	Sol-gel	2 wt% ZrP coated - $LiNi_{0.5}Mn_{1.5}O_4$	~120, 94.6% (200, 1C, 55 °C)	[228]
$LiNbO_3$	Solid-state	1 wt% Li_2NbO_3 coated $LiNi_{0.5}Mn_{1.5}O_4$	~110, 86.8%(150, 1C, 55 °C)	[229]
Li_2SiO_3	Sol-gel	$0.9LiNi_{0.5}Mn_{1.5}O_4{\cdot}0.1Li_2SiO_3$	~100, 85.3%(100, 1C)	[232]
Li_2SnO_3	Sol-gel	1 wt% Li_2SnO_3 coated $LiNi_{0.5}Mn_{1.5}O_4$	~110, 86.8%(150, 1C, 55 °C)	[233]
Li_2TiO_3	Sol-gel	5% Li_2TiO_3 coated - $LiNi_{0.5}Mn_{1.5}O_4$	120, 94.1%(50, 1C, 55 °C)	[234]
$Li_4Ti_5O_{12}$	solvothermal method	5 wt% $Li_4Ti_5O_{12}$ coated $LiNi_{0.5}Mn_{1.5}O_4$	112.8, 93.6% (100, 0.5C)	[236]

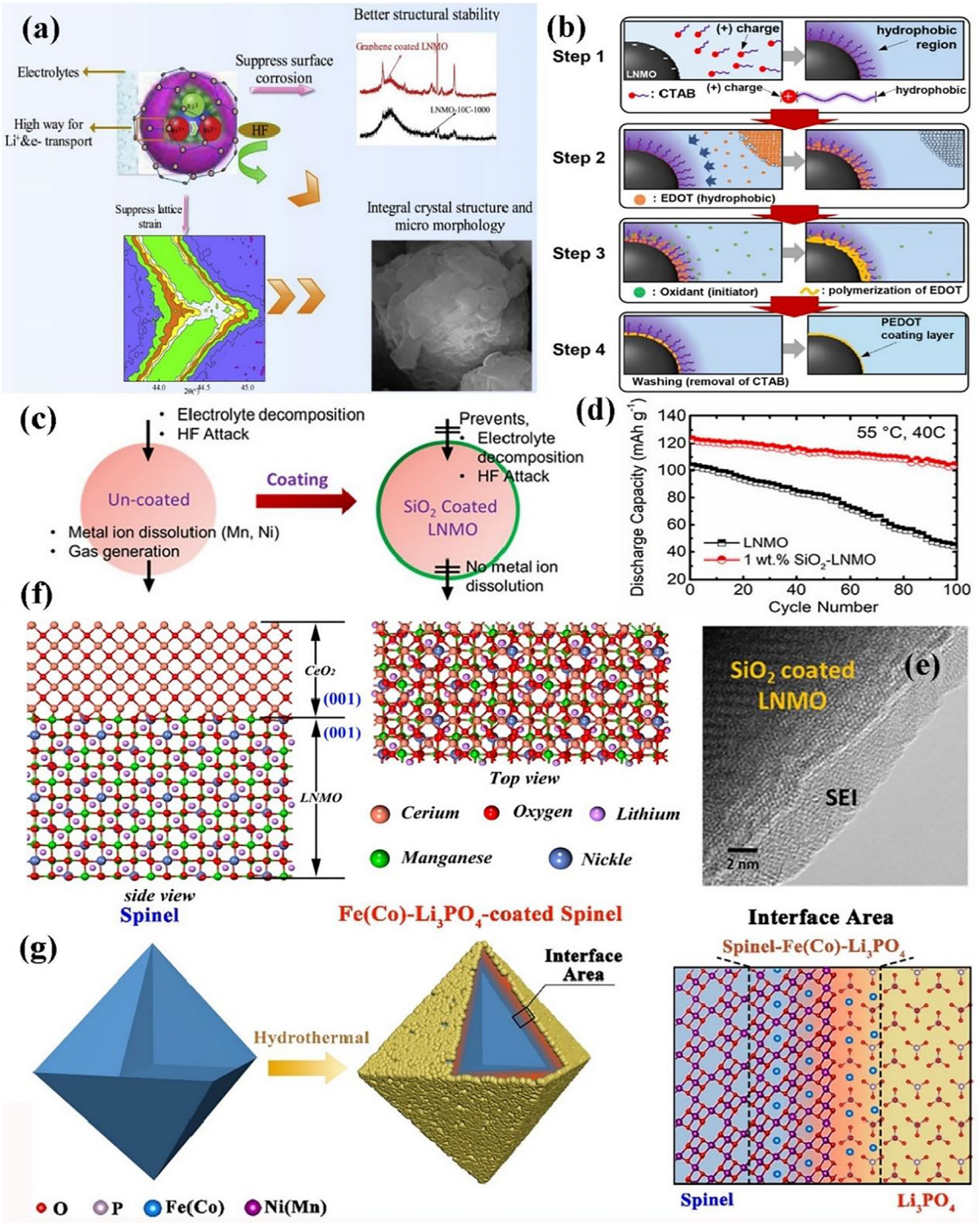

Fig. 12. (a) Mechanism of cycling stability improvement for graphene coated $LiNi_{0.5}Mn_{1.5}O_4$ [209]; (b) schematic diagram of the synthesis process for PEDOT-coated $LiNi_{0.5}Mn_{1.5}O_4$ [211]; (c) mechanism of cycling stability improvement, (d) cycling stability and (e) HRTEM image after cycling for SiO_2 coated $LiNi_{0.5}Mn_{1.5}O_4$ [213]; (f) interface model between $LiNi_{0.5}Mn_{1.5}O_4$ and CeO_2 [214]; (g) schematic diagram of Li_3PO_4 coating mechanism of $LiNi_{0.5}Mn_{1.5}O_4$ [225]. Reproduced from Refs. [209,214] with permission from Elsevier. Reproduced from Refs. [211,213,225] with permission from the American Chemical Society.

temperature. The coated AlF_3 layer can effectively suppress electrolyte decomposition, dissolution of Ni or Mn ions.

Phosphates have been promising coating materials for $LiNi_{0.5}Mn_{1.5}O_4$ because the strong P=O bonds can endow excellent chemical resistance to the coated $LiNi_{0.5}Mn_{1.5}O_4$ against acidic electrolytes [224]. The strong covalence of the PO_4 group can improve the thermal stability of the coated $LiNi_{0.5}Mn_{1.5}O_4$ [224,225]. Wu et al. [225] synthesized Li_3PO_4-coated $LiNi_{0.5}Mn_{1.5}O_4$ by a hydrothermal process. The Li_3PO_4 coating mechanism on $LiNi_{0.5}Mn_{1.5}O_4$ surface by diffusion of bridging ions into the surface is shown in Fig. 12(g). The bridging ions, such as Fe and Co, can migrate into the 16c positions of the $LiNi_{0.5}Mn_{1.5}O_4$ surface to form a bridge layer that connects the $LiNi_{0.5}Mn_{1.5}O_4$ and Li_3PO_4 layers, leading to the dense and uniform coating of $LiNi_{0.5}Mn_{1.5}O_4$ with Li_3PO_4 particles. The Li_3PO_4-coated $LiNi_{0.5}Mn_{1.5}O_4$ indicates a high capacity retention of about 87% and high mean coulombic efficiency of about 98%, but they are ~60% and ~96% for the pristine $LiNi_{0.5}Mn_{1.5}O_4$ after 100 cycles at 55 °C. Xu et al. [226] prepared

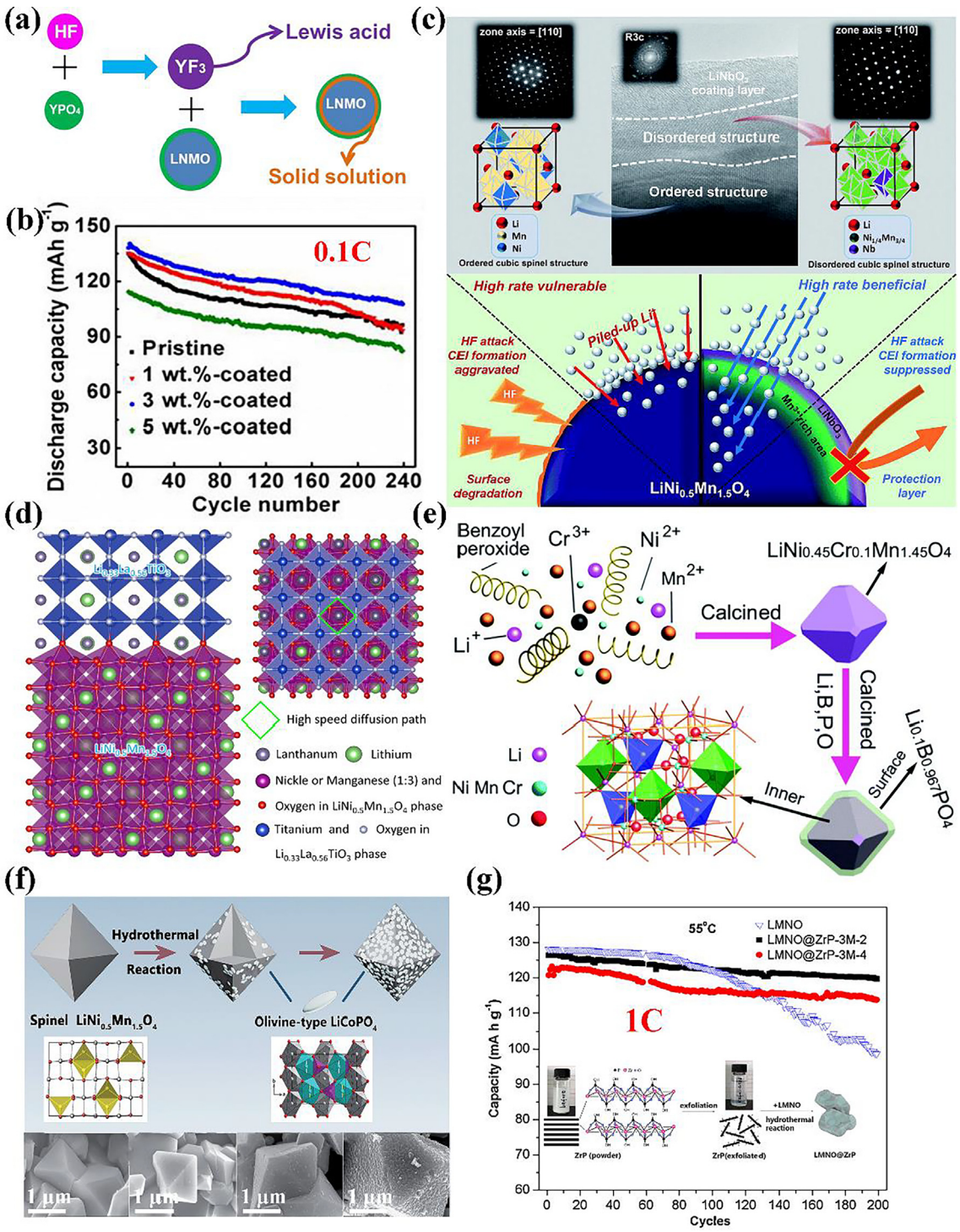

Fig. 13. (a) Mechanism of performance improvement and (b) cycle performance for YPO_4 coated $LiNi_{0.5}Mn_{1.5}O_4$ [226]; (c) schematic diagram of the influence of Nb^{5+} doping on the surface structure and role of the $LiNbO_3$ coating film on the surface of $LiNi_{0.5}Mn_{1.5}O_4$ [229]; (d) interfacial model between $LiNi_{0.5}Mn_{1.5}O_4$ and $Li_{0.33}La_{0.56}TiO_3$ [230]; (e) schematic diagram of the synthesis process for LBPO-coated $LiCr_{0.1}Ni_{0.45}Mn_{1.45}O_4$ [231]; (f) schematic illustration of the synthesis process and SEM images of $LiNi_{0.5}Mn_{1.5}O_4$@ $LiCoPO_4$ (0 wt%, 1 wt%, 5 wt% and 10 wt%) [235]; (g) cycle performance of pristine $LiNi_{0.5}Mn_{1.5}O_4$ and ZrP coated one at elevated temperature (inset is the synthesis process of ZrP coated $LiNi_{0.5}Mn_{1.5}O_4$) [228]. Reproduced from Ref. [226] with permission from the American Chemical Society. Reproduced from Reproduced from Refs. [228,230] with permission from Elsevier. Refs. [229,231,235] with permission from The Royal Society of Chemistry.

$LiNi_{0.5}Mn_{1.5}O_4$ via a sol–gel route, and then synthesized YPO_4-coated $LiNi_{0.5}Mn_{1.5}O_4$ through a facile wet chemical method. An ion exchange between PO_4^{3-} and F^- can be found, and YF_3 Lewis acid can be generated on $LiNi_{0.5}Mn_{1.5}O_4$ surface (Fig. 13a). The formed YF_3 layer can accelerate surface ion transportation and then enhance the electrochemical properties. The YPO_4 (3 wt%)-coated $LiNi_{0.5}Mn_{1.5}O_4$ indicates a high reversible capacity of 94 mAh g^{-1} and good cycle performance with a capacity retention of 77.5% at 0.1C after 240 cycles, which are obviously higher than pristine $LiNi_{0.5}Mn_{1.5}O_4$ (Fig. 13b).

Nonetheless, it has been reported that the phosphates tend to be discontinuously deposited on the surface of $LiNi_{0.5}Mn_{1.5}O_4$ par-

ticles, resulting in uneven coating layer. Hu et al. [228] designed a novel way to synthesize layered α-ZrP-coated $LiNi_{0.5}Mn_{1.5}O_4$. The $LiNi_{0.5}Mn_{1.5}O_4$ was prepared by a sol–gel process, and 10 g of $ZrOCl_2{\cdot}8H_2O$ was refluxed with 100 ml of 3 mol L^{-1} H_3PO_4 at 100 °C for 24 h to prepare ZrP (noted as ZrP-3 M). Then, the mixture of ZrP and $LiNi_{0.5}Mn_{1.5}O_4$ reacted in sealed teflon-lined pressure vessel at 160 °C for 15 h, and then ZrP nanosheets deposited on the surface of $LiNi_{0.5}Mn_{1.5}O_4$ particles (Inset of Fig. 13g). 2 wt % ZrP-3 M−coated $LiNi_{0.5}Mn_{1.5}O_4$ is named as LMNO@ZrP-3 M−2. The LMNO@ZrP-3 M−2 shows a high reversible capacity of ~120 mAh g^{-1} and good cycle performance with a capacity retention of ~95% at 1C at 55 °C after 200 cycles, which are obviously higher than pristine $LiNi_{0.5}Mn_{1.5}O_4$ (Fig. 13g).

The traditional inorganic coating materials often show low lithium-ion conductivity and electronic conductivity, which lead to a possible increase of the charge transfer resistance cycled at high current densities. To conquer these problems, some Li-ion conductors have recently been used as coating materials to improve the electrochemical performance of $LiNi_{0.5}Mn_{1.5}O_4$. For instance, Kim et al. [229] developed a new way to synthesize $LiNbO_3$ coated $LiNi_{0.5}Mn_{1.5}O_4$, which indicated excellent electrochemical property. As shown in Fig. 13(c), the Mn^{3+}-dominant region near the $LiNi_{0.5}Mn_{1.5}O_4$ surface can offer extra electron hopping paths, and then leads to a rapid charge transfer in $LiNi_{0.5}Mn_{1.5}O_4$. As an ion conductor, the coated $LiNbO_3$ film promotes the Li ion migration, restrain the side reaction at the cathode/electrolyte interface during the charge process. $LiNbO_3$ (1 wt%) coated $LiNi_{0.5}Mn_{1.5}O_4$ indicates high reversible capacity of about 120 mAh g^{-1} at 0.5C even at 60 °C after 100 cycles, whereas the capacity of pristine one is close to zero. Zhu et al. [230] designed a novel $LiNi_{0.5}Mn_{1.5}O_4$@$Li_{0.33}La_{0.56}TiO_3$ composites synthesized by a sol–gel process, and the $LiNi_{0.5}Mn_{1.5}O_4$@$Li_{0.33}La_{0.56}TiO_3$ (3 wt%) showed a high discharge capacity and a good rate performance. As shown in Fig. 13(d), the lithium ion in $Li_{0.33}La_{0.56}TiO_3$ can move quickly because of the relatively low Li contents at the local environment. The high ionic conductivity of $Li_{0.33}La_{0.56}TiO_3$ can reduce the interfacial charge transfer impedances, resulting in the improvement of the diffusion rate of lithium ions in the composites. Hence, the overall impedance decreases and the electrochemical performance is improved. Yang et al. [231] synthesized Cr-doped $LiNi_{0.5}Mn_{1.5}O_4$ ($LiCr_{0.1}Ni_{0.45}Mn_{1.45}O_4$) by a combustion method, and then prepared $Li_{0.1}B_{0.967}PO_4$ (LBPO)-coated $LiCr_{0.1}Ni_{0.45}Mn_{1.45}O_4$ used benzoyl peroxide as oxidizer (Fig. 13e). The (LBPO)-coated $LiCr_{0.1}Ni_{0.45}Mn_{1.45}O_4$ shows a discharge capacity of about 125 mAh g^{-1} and a high capacity retention of about 91% at 1C rate after 400 cycles, which are higher than those of $LiNi_{0.5}Mn_{1.5}O_4$ (101 mAh g^{-1} and 74.5%).

The motive for coating $LiNi_{0.5}Mn_{1.5}O_4$ by another electrode material is to obtain a more balanced electrochemical property compared to what is possible with any single material. For example, $LiCoPO_4$ coating can improve the energy density of $LiNi_{0.5}Mn_{1.5}O_4$ due to its high potential plateau (about 4.8 V) and high theoretical capacity of 167 mA h g^{-1}. Liu et al. [234] prepared $LiCoPO_4$ coated $LiNi_{0.5}Mn_{1.5}O_4$ with a particle size of 1–2 μm by a hydrothermal process (Fig. 13f). $LiCoPO_4$ (5 wt%) coated $LiNi_{0.5}Mn_{1.5}O_4$ exhibits the most excellent electrochemical property with a discharge capacity of 132 mAh g^{-1} at 0.5C after 100 cycles and 130 mAh g^{-1} 20C.

In general, the dissolution of transition metal ions makes the serious capacity fading of spinel Mn-based cathode materials, especially at evaluated temperature. The delicate morphology can enhance the cycling stability, especially nanostructured spinels, which can shorten diffusion pathway of ions and electrons and alleviate the volume change during cycling. In addition, different surface inclinations can result in different stability and Mn dissolution rates at surfaces, which provides a practical way to control the morphology and crystal orientation of the spinels. Doping is one of the most common ways to enhance the cycle stability of spinel Mn-based cathode materials. Given the disproportionation mechanism of Mn^{3+} in $LiMn_2O_4$, an effective strategy is to increases the average valence state of Mn via lower-valence (less than or equal to +3) cation doping, and inhibits the Jahn-Teller effect. Using rare earth elements to dope $LiMn_2O_4$ at Mn site or Na doping at Li site can also improve the cycling stability of $LiMn_2O_4$ because the big ionic radius can broaden the lithium ion migration channel. In addition, the high-valence (greater than +3) cation doping (such as Ti^{4+}) and anion substitution of O^{2-} by F^- have also been reported to improve the cycle stability of $LiMn_2O_4$, which seems to violate common sense due to the reduction of average valence state of Mn. The performance improvement may be related to the alteration of surface structure or chemical bond. For example, the Mn–F bond energy is generally larger than that of Mn–O bond energy, and then improve the structure stability of $LiMn_2O_4$. In addition, the doping with electrochemically active nickel element results in the development of $LiNi_{0.5}Mn_{1.5}O_4$ with higher discharge voltage platform and higher energy density than $LiMn_2O_4$. The doping was regarded as an effective strategy to enhance the electrical conductivity and lithium-ion diffusion coefficient of $LiNi_{0.5}Mn_{1.5}O_4$. The surface coating can effectively avoid the direct contact between spinel cathode and electrolyte and restrain side reactions such as Mn or Ni dissolution. To ensure the interface stability, a perfect coating layer should possess a good lattice match with spinel cathodes and be an excellent lithium ion and electronic conductor. Hence, coating spinel cathodes with fast lithium ion conductors has received wide attention. In addition, it is significant to obtain homogeneous thin coating with excellent wettability, which maintains stable morphology and structure not only in the pristine state but also during electrochemical cycling.

6. Summary and outlook

As promising cathode materials for high-performance LIBs, Mn-based oxides are of great importance because of the high theoretical capacity, low cost, and environmentally benign nature. However, the practical applications have been limited because of severe capacity deterioration (such as $LiMnO_2$ and $LiMn_2O_4$ from the Jahn-Teller effect of Mn^{3+}) as well as further complications from successive structure changes during cycling, low initial coulombic efficiency (such as Li-rich cathode and $LiNi_{0.5}Mn_{1.5}O_4$) and oxidization of organic carbonate solvents at high charge potential. Large amounts of efforts have been concentrated on resolving these issues towards practical applications, and many vital progresses have been carried out. In this review, the primary target is focused on different proposed strategies and breakthroughs to enhance the rate performance and cycling stability of nanostructured Mn-based oxide cathode materials for LIBs, including morphology control, ion doping, surface coatings, composite construction, etc.

The electrochemical property of Mn-based oxide materials could be enhanced by designing 1D, 2D and 3D nanostructures. 1D nanostructures offer a direct migration path of ion and electron, improve the contact area between active materials and electrolyte, and alleviate volume change, and then improves the electrochemical performance of Mn-based oxide electrodes. Because of the intrinsic characteristic of large surface area, unusual electronic performance and ultrathin thickness compared with the diameter of one-dimensional nanostructures, 2D Mn-based oxide materials can be expected to exhibit even more excellent electrochemical performance than 1D Mn-based oxide materials. Furthermore, 2D nanostructures can assemble into

three-dimensional structure such as nanoflower composed of nanosheets. Beyond 1D and 2D nanostructures, 3D structure possesses particular performances because they possess the merits of most related nanoscale building-blocks, such as high specific surface area, large defect density and cellular structure. In addition, 3D structure Mn-based oxide materials can easily achieve high energy density used in LIBs because of the large surface/volume ratios.

Doping is one of the most common ways to enhance the cycle stability of spinel Mn-based cathode materials. For Mn-based Li rich materials, the doping is an effective strategy to decrease voltage decay by blocking of transition metal ions migration and the stabilizing the transition metal and oxygen atom layers. The doping also can reduce the cation intermixing by altering the local coordination environment and oxygen activity, and then reduce oxygen evolution and lithium loss in Mn-based Li rich materials. For $LiMn_2O_4$, an effective strategy is to increases the average valence state of Mn via lower-valence cation doping, and inhibits the Jahn-Teller effect. In addition, the doping with electrochemically active nickel element results in the development of $LiNi_{0.5}Mn_{1.5}O_4$ with higher discharge voltage platform and higher energy density than $LiMn_2O_4$. The doping was regarded as an effective strategy to enhance the electrical conductivity and lithium ion diffusion coefficient of $LiNi_{0.5}Mn_{1.5}O_4$.

The surface coating can alleviate the side reaction at electrode/-electrolyte interface, decrease the surface lattice oxygen evolution, and then increase retention of oxide ion vacancy in the lattice after the first charge. To ensure the interface stability, a perfect coating layer should possess a good lattice match with spinel cathodes and be an excellent lithium ion and electronic conductor. Hence, coating spinel cathodes with fast lithium ion conductors has received wide attention. In addition, it is significant to obtain homogeneous thin coating with excellent wettability, which maintains stable morphology and structure not only in the pristine state but also during electrochemical cycling.

The performance enhancement strategy mentioned above has its relative merits and disadvantages. The morphology control can reduce the transmission pathway of lithium ions and electrons based on the ion diffusion equation, and then improve the electrochemical performance of electrode materials. However, the easy aggregation, low tap density of nanostructured materials and the uncontrollable side reactions between active materials and electrolyte while loading the electrodes requires further corresponding design for developing high-performance cathodes. Surface coating or composite construction with a conductive layer is an effective strategy to improve the conductivity of electrode materials, enhance interfacial stability between electrode and electrolyte, and restrain transitional metals dissolution in the HF-containing electrolyte. However, a uniform surface coating around the whole particle of electrode materials is difficult to achieve. The element doping can enhance the inherent conductivity of electrode materials by altering the bond strength and the local environment of the lattice, creating gaps, enhancing the stability of the primary skeleton, or altering ion inter-atomic forces to promote the ions transmission. However, the doping usually reduces the number of active ions, and then decreases the reversible capacity, especially initial capacity. In addition, the real working principle of various doping elements need to be quantitatively evaluated. A combination between morphology control and surface coatings, composite construction, ion doping may be a more effective strategy to achieve deeper insight into the structure-performance issues, which contribute to the rational design and structure optimization of Mn-based cathode materials.

For $LiMnO_2$, a major challenge is the irreversible and progressive structure change from the layered structure to a spinel structure. For Mn-based Li-rich cathodes, the major challenges include low initial coulombic efficiency, severely continuous voltage decay and transitional metals dissolution. For $LiMn_2O_4$, the dissolution of Mn^{3+} is one of the most important factors for the capacity decay because of the inevitable Jahn–Teller effect. The $LiNi_{0.5}Mn_{1.5}O_4$ suffers from the aggressive electrolyte oxidation at the later stage of charging and the transitional metals dissolution in the HF-containing electrolyte, resulting in serious structure deterioration. To resolve these challenges, many efficient ways have been used to improve the electrochemical performances of Mn-based oxide cathodes. A scientifical investigation on key factors influencing the cell performance is essential, which includes synthesis route of the cathode materials, the location valance state of doping ions, kinds and thickness of coating materials, match of the electrolyte, membrane, kinds of conductive additive and binders. A combination between electrochemical in-situ technology and first-principle calculation route is an effective strategy to achieve deeper insight into the structure-performance issues, which contribute to the rational design and structure optimization of Mn-based cathode materials. A further study of the doping and surface coating mechanism should be studied, which can directly optimize the physical and chemical performance of Mn-based oxide cathodes.

As the flourish of the hybrid electrical vehicles, electric vehicles, and energy storage devices, the challenge is the development of Li-ion batteries with a dramatically extended life span and much-increased energy density. In summary, Mn-based oxide cathodes, are still one of the hopeful alternatives for high-performance Li-ion batteries. Therefore, it is significant to gain Mn-based oxide cathodes with a balance among different factors in order to further facilitate industrialized application in the field of LIBs. Hence, the combination of basic and applied research seems to be very important. In addition, to obtain a more extensive range of commercial applications, the green, cheap and controllable synthesis routes to prepare Mn-based oxide cathode materials with good performance need to be further developed. Especially, developing the Mn-based Li-rich cathodes with high specific capacity (>250 mAh g^{-1}) and high energy density (>1000 Wh kg^{-1}) is a promising research direction, which can meet the requirement of the automotive market to achieve long-distance drive (>300 miles) and low cost.

Declaration of Competing Interest

The authors declare that they have no known competing financial interests or personal relationships that could have appeared to influence the work reported in this paper.

Acknowledgments

This work was financially supported by the National Natural Science Foundation of China (no. 51672120), the Scientific Research Project of Mudanjiang Normal University (no. 1355JG014), the Natural Science Foundation of Hebei Province of China (no. B2020501003), and the Fundamental Research Funds for the Central Universities (no. N2023030).

References

[1] T.-F. Yi, T.-T. Wei, Y. Li, Y.-B. He, Z.-B. Wang, Energy Storage Mater. 26 (2020) 165–197.
[2] X. Qu, Z. Yu, D. Ruan, A. Dou, M. Su, Y. Zhou, Y. Liu, D. Chu, ACS Sustain. Chem. Eng. 8 (2020) 5819–5830.
[3] S.J. Hu, A.S. Pillai, G.M. Liang, W.K. Pang, H.Q. Wang, Q.Y. Li, Z.P. Guo, Electrochem. Energy Rev. 2 (2019) 277–311.
[4] K. Zhang, B. Li, Y.X. Zuo, J. Song, H.F. Shang, F.H. Ning, D.G. Xia, Electrochem. Energy Rev. 2 (2019) 606–623.

[5] T.-F. Yi, P.-P. Peng, Z.K. Fang, Y.-R. Zhu, Y. Xie, S.H. Luo, Compos. Part B Eng. 175 (2019) 107067.
[6] A.-H. Marincaș, F. Goga, S.-A. Dorneanu, P. Ilea, J. Solid State Electrochem. 24 (2020) 473–497.
[7] T.-F. Yi, Y. Li, Z.K. Fang, P. Cui, S.H. Luo, Y. Xie, J. Mater. 6 (2020) 33–44.
[8] T. Ohzuku, S. Takeda, M. Iwanaga, J. Power Sources 81–82 (1999) 90–94.
[9] Y. Xie, H.-T. Yu, T.-F. Yi, Y.-R. Zhu, ACS Appl. Mater. Interface 6 (2014) 4033–4042.
[10] Z. Yu, X. Qu, T. Wan, A. Dou, Y. Zhou, X. Peng, M. Su, Y. Liu, D. Chu, ACS Appl. Mater. Interfaces 12 (2020) 40393–40403.
[11] J. Abou-Rjeily, I. Bezza, N.A. Laziz, C. Autret-Lambert, M.T. Sougrati, F. Ghamouss, Energy Storage Mater. 26 (2020) 423–432.
[12] J.H. Kim, S.T. Myung, C.S. Yoon, S.G. Kang, Y.K. Sun, Chem. Mater. 16 (2004) 906–914.
[13] Y.-R. Zhu, T.-F. Yi, Ionics 22 (2016) 1759–1774.
[14] Z.-F. Huang, X. Meng, C.-Z. Wang, Y. Sun, G. Chen, J. Power Sources 158 (2006) 1394–1400.
[15] Q. Zhong, A. Bonakdarpour, M. Zhong, Y. Gao, J.R. Dahn, J. Electrochem. Soc. 144 (1997) 205–213.
[16] Z.X. Nie, C.Y. Ouyanga, J.Z. Chenc, Z.Y. Zhong, Y.L. Du, D.S. Liu, S.Q. Shi, M.S. Lei, Solid State Commun. 150 (2010) 40–44.
[17] T.-F. Yi, J. Mei, Y.-R. Zhu, J. Power Sources 316 (2016) 85–105.
[18] X. Xu, S. Lee, S. Jeong, Y. Kim, J. Cho, Mater. Today 16 (2013) 487–495.
[19] Y. Fang, X.-Y. Yu, X.W. Lou, Matter 1 (2019) 90–114.
[20] H.M. Ji, G. Yang, X.W. Miao, A.Q. Hong, Electrochim. Acta 55 (2010) 3392–3397.
[21] T.-J. Kim, D. Son, J. Cho, B. Park, J. Power Sources 154 (2006) 268–272.
[22] Y. Wang, H. Li, P. He, E. Hosono, H. Zhou, Nanoscale 2 (2010) 12941305.
[23] Q. Liu, D.L. Mao, C.K. Chang, F.Q. Huang, J. Power Sources 173 (2007) 538–544.
[24] F. Zhou, X.M. Zhao, Y.Q. Liu, L. Li, C.G. Yuan, J. Phys. Chem. Solids 69 (2008) 2061–2065.
[25] Y. He, R.H. Li, X.K. Ding, L.L. Jiang, M.D. Wei, J. Alloy Compd. 492 (2010) 601–604.
[26] H.M. Ji, X.W. Miao, L. Wang, B. Qian, G. Yang, ACS Sustain. Chem. Eng. 2 (2014) 359–366.
[27] H.Y. Zhao, B. Chen, C. Cheng, W.Q. Xiong, Z.W. Wang, Z. Zhang, L.P. Wang, X.Q. Liu, Ceram. Int. 41 (2015) 15266–15271.
[28] Y. He, Q. Feng, S.Q. Zhang, Q.L. Zou, X.L. Wu, X.J. Yang, ACS Sustain. Chem. Eng. 1 (2013) 570–573.
[29] A. Boulineau, L. Croguennec, C. Delmas, F. Weill, Solid State Ionics 180 (2010) 1652–1659.
[30] O. Toprakci, H.A.K. Toprakci, Y. Li, L.W. Ji, L.G. Xue, H. Lee, S. Zhang, X.W. Zhang, J. Power Sources 241 (2013) 522.
[31] T.-F. Yi, W. Tao, B. Chen, Y.-R. Zhu, S.-Y. Yang, Y. Xie, Electrochim. Acta 188 (2016) 686–695.
[32] C.-H. Shen, Q. Wang, F. Fu, L. Huang, Z. Lin, S.-Y. Shen, H. Su, X.-M. Zheng, B.-B. Xu, J.-T. Li, S.-G. Sun, ACS Appl. Mater. Interfaces 6 (2014) 5516–5524.
[33] Y. Jiang, Z. Yang, W. Luo, X.L. Hu, Y.H. Huang, Phys. Chem. Chem. Phys. 15 (2013) 2954–2960.
[34] W.C. Duan, Z. Hu, K. Zhang, F.Y. Cheng, Z.L. Tao, J. Chen, Nanoscale 5 (2013) 6485–6490.
[35] X.W. Miao, Y. Yan, C.G. Wang, L.L. Cui, J.H. Fang, G. Yang, J. Power Sources 247 (2014) 219–227.
[36] B.L. Guan, S.-Y. Qi, Y. Li, T. Sun, Y.-G. Liu, T.-F. Yi, J. Energy Chem. 54 (2021) 680–698.
[37] M.G. Kim, M.K. Jo, Y.-S. Hong, J. Cho, Chem. Commun. (2009) 218–220.
[38] E. Hosono, T. Saito, J. Hoshino, Y. Mizuno, M. Okubo, D. Asakur, K. Kagesaw, D. Nishio-Hamane, T. Kudo, H.S. Zhou, CrystEngComm 15 (2013) 2592–2597.
[39] Y. Lee, M.G. Kim, J. Cho, Nano Lett. 8 (2008) 957–961.
[40] J.G. Yang, F.Y. Cheng, X.L. Zhang, H.Y. Gao, Z.L. Tao, J. Chen, J. Mater. Chem. A 2 (2014) 1636–1640.
[41] X. He, J. Wang, R. Wang, B. Qiu, H. Frielinghaus, P. Niehoff, H.D. Liu, M.C. Stan, E. Paillard, M. Winter, J. Li, J. Mater. Chem. A 4 (2016) 7230–7237.
[42] F. Fu, J.Y. Tang, Y.Z. Yao, M.H. Shao, ACS Appl. Mater. Interfaces 8 (2016) 25654–25659.
[43] F. Yang, Q.G. Zhang, X.H. Hu, T.Y. Peng, Electrochim. Acta 165 (2015) 182–190.
[44] R. Qing, J. Shi, D. Xiao, X. Zhang, Y. Yin, Y. Zhai, L. Gu, Y. Guo, Adv. Energy Mater. 6 (2016) 1501914.
[45] M. Lou, S.-S. Fan, H.-T. Yu, Y. Xie, Q.Y. Zhang, Y.-R. Zhu, T.-F. Yi, G.-H. Tian, J. Alloy Compd. 739 (2018) 607–615.
[46] Y.G. Sorboni, H. Arabi, A. Kompany, Ceram. Int. 45 (2019) 2139–2145.
[47] X. Wei, P. Yang, H. Li, S. Wang, Y. Xing, X. Liu, S. Zhang, RSC Adv. 7 (2017) 35055–35059.
[48] B. Song, C. Zhou, H. Wang, H. Liu, Z. Liu, M.O. Lai, L. Lu, J. Electrochem. Soc. 161 (2014) A1723–A1730.
[49] T.F. Yi, Y.M. Li, S.Y. Yang, Y.R. Zhu, Y. Xie, ACS Appl. Mater. Interfaces 8 (2016) 32349–32359.
[50] T.-F. Yi, X. Han, S.Y. Yang, Y.R. Zhu, Sci. China Mater. 59 (2016) 618–628.
[51] R. Yu, G. Wang, M. Liu, X. Zhang, X. Wang, H. Shu, X. Yang, W. Huang, J. Power Sources 335 (2016) 65–67.
[52] T.L. Zhao, R.X. Ji, H.B. Yang, Y.X. Zhang, X.G. Sun, Y.T. Li, L. Li, R.J. Chen, J. Energy Chem. 33 (2019) 37–45.
[53] X. Feng, Y. Gao, L. Ben, Z. Yang, Z. Wang, L. Chen, J. Power Sources 317 (2016) 74–80.
[54] H. Chen, Q. Hu, Z. Huang, Z. He, Z. Wang, H. Guo, X. Li, Ceram. Int. 42 (2016) 263–269.
[55] B. Song, M.O. Lai, L. Lu, Electrochim. Acta 80 (2012) 187–195.
[56] Z.P. Ding, M.Q. Xu, J.T. Liu, Q. Huang, L.B. Chen, P. Wang, D.G. Ivey, W.F. Wei, ACS Appl. Mater. Interfaces 9 (2017) 20519–20526.
[57] B. Li, X.B. Wang, Y.B. Gao, B. Wang, J.X. Qiu, X. Cheng, D.M. Dai, J. Mater. 5 (2019) 149–155.
[58] Y.Y. Sun, Q. Wu, L. Zhao, Ceram. Int. 45 (2019) 1339–1347.
[59] L. Li, B.H. Song, Y.L. Chang, H. Xia, J.R. Yang, K.S. Lee, L. Lu, J. Power Sources 283 (2015) 162–170.
[60] B. Li, H. Yan, J. Ma, P. Yu, D. Xia, W. Huang, W. Chu, Z. Wu, Adv. Funct. Mater. 24 (2014) 5112–5118.
[61] J.L. Shi, R. Qi, X.D. Zhang, P.F. Wang, W.G. Fu, Y.X. Yin, J. Xu, L.J. Wan, Y.G. Guo, ACS Appl. Mater. Interfaces 9 (2017) 42829–42835.
[62] M. Hagen, W.J. Cao, A. Shellikeri, D. Adams, X.J. Chen, W. Brandt, S.R. Yturriaga, Q. Wu, J.A. Read, T.R. Jow, J.P. Zheng, J. Power Sources 379 (2018) 212–218.
[63] P. Guan, L. Zhou, Z. Yu, Y. Sun, Y. Liu, F. Wu, Y. Jiang, D. Chu, J. Energy Chem. 43 (2020) 220–235.
[64] Q.B. Xia, X.F. Zhao, M.Q. Xu, Z.P. Ding, J.T. Liu, L.B. Chen, D.G. Ivey, W.F. Wei, J. Mater. Chem. A 3 (2015) 3995–4003.
[65] T.-F. Yi, L.Y. Qiu, J. Mei, S.Y. Qi, P. Cui, S.H. Luo, Y.-R. Zhu, Y. Xie, Y.B. He, Sci. Bull. 65 (2020) 546–556.
[66] F. Wu, J.R. Liu, L. Li, X.X. Zhang, R. Luo, Y.S. Ye, R.J. Chen, ACS Appl. Mater. Interfaces 8 (2016) 23095–23104.
[67] Z. Yang, J.J. Zhong, J.L. Li, Y.Y. Liu, B. Niu, F.Y. Kang, Ceram. Int. 45 (2019) 439–448.
[68] J. Li, J. Li, T. Yu, F. Ding, G. Xu, Z. Li, Y. Zhao, F. Kang, Ceram. Int. 42 (2016) 18620–18630.
[69] Y. Jung, A.S. Cavanagh, Y. Yan, S.M. George, J. Electrochem. Soc. 158 (2011) A1298–A1302.
[70] S. Zhang, H. Gu, T. Tang, W. Du, M. Gao, Y. Liu, D. Jian, H. Pan, ACS Appl. Mater. Interfaces 9 (2017) 33863–33875.
[71] C. Chen, T. Geng, C. Du, P. Zuo, X. Cheng, Y. Ma, G. Yin, J. Power Sources 331 (2016) 91–99.
[72] Y. Gao, Z.Y. Shang, X.Q. He, T. White, J. Park, X.H. Liang, Electrochim. Acta 318 (2019) 513–524.
[73] G.R. Hu, Z.C. Xue, Z.Y. Luo, Z.D. Peng, Y.B. Cao, W.G. Wang, Y.X. Zeng, Y. Huang, Y. Tao, T.F. Li, Z.Y. Zhang, K. Du, Ceram. Int. 45 (2019) 10633–10639.
[74] J.Z. Kong, H.F. Zhai, X. Qian, M. Wang, Q.Z. Wang, A.D. Li, H. Li, F. Zhou, J. Alloy. Compd. 694 (2017) 848–856.
[75] X.F. Zhang, I. Belharouak, L. Li, L. Lei, A. Nei, X.Q. Chen, R.S. Yassar, R.L. Axelbaum, Adv. Energy Mater. 3 (2013) 1299–1307.
[76] S. Shi, J. Tu, Y. Zhang, Electrochim. Acta 108 (2013) 441–448.
[77] Z. Wang, E.Z. Liu, L.C. Guo, C.S. Shi, C.N. He, N.Q. Zhao, Surf. Coat. Technol. 235 (2013) 570–576.
[78] L. Zhou, M.J. Tian, Y.L. Deng, Q.J. Zheng, C.G. Xu, D.M. Lin, Ceram. Int. 42 (2016) 15623–15633.
[79] X.Y. Liu, J.L. Liu, T. Huang, A.S. Yu, Electrochim. Acta 109 (2013) 52–58.
[80] S. Sun, N. Wan, Q. Wu, Solid State Ionics 278 (2015) 85–90.
[81] C.D. Li, J. Xu, J.S. Xia, W. Liu, X. Xiong, Z.A. Zheng, Solid State Ionics 292 (2016) 75–82.
[82] C. Lu, H. Wu, Y. Zhang, H. Liu, B.J. Chen, J. Power Sources 267 (2014) 682–691.
[83] J. Zheng, M. Gu, J. Xiao, B.J. Polzin, P. Yan, X.L. Chen, C.M. Wang, J.G. Zhang, Chem. Mater. 26 (2014) 6320–6327.
[84] X.F. Bian, Q. Fu, X.F. Bie, P.L. Yang, H.L. Qiu, Q. Pang, G. Chen, F. Du, Y.J. Wei, Electrochim. Acta 174 (2015) 875–884.
[85] H. Liu, C. Chen, C. Du, X.S. He, G.P. Yin, B. Song, P.J. Zuo, X.Q. Cheng, J. Mater. Chem. A 3 (2015) 2634–2641.
[86] Z. Wang, E. Liu, C. He, C.S. Shi, J.J. Li, N.Q. Zhao, J. Power Sources 236 (2013) 25–32.
[87] F. Wu, X. Zhang, T. Zhao, ACS Appl. Mater. Interfaces 7 (2015) 3773–3781.
[88] B. Xiao, B. Wang, J. Liu, K. Kaliyappan, Q. Sun, Y. Liu, G. Dadheech, M.P. Balogh, L. Yang, T.K. Sham, R. Li, M. Cai, X. Sun, Nano Energy 34 (2017) 120–130.
[89] F. Ding, J. Li, F. Deng, G. Xu, Y. Liu, K. Yang, F. Kang, ACS Appl. Mater. Interfaces 9 (2017) 27936–27945.
[90] L. He, J. Xu, T. Han, H. Han, Y. Wang, J. Yang, J. Wang, W. Zhu, C. Zhang, Y. Zhang, Ceram. Int. 43 (2017) 5267–5273.
[91] D.D. Wang, T.H. Xu, Y.P. Li, D. Pan, L. Li, Y. Bai, Ceram. Int. 44 (2018) 17425–17433.
[92] X. Zhang, S. Sun, Q. Wu, N. Wan, D. Pan, Y. Bai, J. Power Sources 282 (2015) 378–384.
[93] J. Zhang, H. Zhang, R. Gao, Z. Li, Z. Hu, X. Liu, Phys. Chem. Chem. Phys. 18 (2016) 13322–13331.
[94] M. Xu, Q. Lian, Y. Wu, C. Ma, P. Tan, Q. Xia, D.G. Ivey, W. Wei, RSC Adv. 6 (2016) 34245–34253.
[95] D.D. Wang, T.H. Xu, Y.P. Li, D. Pan, X. Lu, Y.S. Hu, S. Dai, Y. Bai, ACS Appl. Mater. Interfaces 10 (2018) (1813) 41802–41804.
[96] M.M. Thackeray, W. David, P.G. Bruce, J.B. Goodenough, Mater. Res. Bull. 18 (1983) 461.
[97] T.-F. Yi, J.J. Pan, T.T. Wei, Y.W. Li, G.Z. Cao, Nano Today 33 (2020) 100894.
[98] C.H. Zheng, X. Liu, Z.F. Wu, Z.D. Chen, D.L. Fang, Electrochim. Acta 111 (2013) 192–199.
[99] V. Aravindan, J. Sundaramurthy, P. Kumar, N. Shubha, W.L. Ling, S. Ramakrishna, S. Madhavi, Nanoscale 5 (2013) 10636.
[100] W.W. Sun, F. Cao, Y.M. Liu, X.Z. Zhao, X.G. Liu, J. Yuan, J. Mater. Chem. 22 (2012) 20952.
[101] C.Y. Zhu, G. Saito, T. Akiyama, Mater. Chem. A 1 (2013) 7077–7082.

[102] H.Y. Zhao, X.Y. Gao, Y.Y. Li, Q. R, C.G. Fu, Y. Feng, J. Liu, X.Q. Liu, J.X. Su, Ceram Int. 45 (2019) 17591–17597.
[103] H.W. Lee, P. Muralidharan, R. Ruffo, C.M. Mari, Y. Cui, D.K. Kim, Nano Lett. 10 (2010) 3852–3856.
[104] Y.L. Ding, J. Xie, G.S. Cao, T.J. Zhu, H.M. Yu, X.B. Zhao, Adv. Funct. Mater. 21 (2011) 348–355.
[105] F.Y. Cheng, H.G. Wang, Z.Q. Zhu, Y. Wang, T.R. Zhang, Z.L. Tao, J. Chen, Energy Environ. Sci. 4 (2011) 3668.
[106] Y. Wu, C.B. Cao, J.T. Zhang, L. Wang, X.L. Ma, X.Y. Xu, ACS Appl. Mater. Interfaces 8 (2016) 19567–19572.
[107] Q.T. Qu, L.J. Fu, X.Y. Zhan, D. Samuelis, J. Maier, L. Li, S. Tian, Z.H. Li, Y.P. Wu, Energy Environ. Sci. 4 (2011) 3985.
[108] S. Jayaraman, V. Aravindan, P.S. Kumar, W.C. Ling, S. Ramakrishna, S. Madhavi, Chem. Commun. 49 (2013) 6677–6679.
[109] J. Luo, Y. Wang, H. Xiong, Y. Xia, Chem. Mater. 19 (2007) 4791–4795.
[110] Y. Qiao, S.R. Li, Y. Yu, C.H. Chen, J. Mater. Chem. A 1 (2013) 860–867.
[111] S.H. Ng, J.Z. Wang, D. Wexler, K. Konstantinov, Z.P. Guo, H.K. Liu, Angew. Chem. Int. Ed. 45 (2006) 6896–6899.
[112] Y. Shi, S.L. Chou, J.Z. Wang, D. Wexler, H.J. Li, H.K. Liu, Y. Wu, J. Mater. Chem. 22 (2012) 16465–16470.
[113] H.K. Noh, H.S. Park, H.Y. Jeong, S.U. Lee, H.K. Song, Angew. Chem. Int. Ed. 126 (2014) 5159–5163.
[114] T.-F. Yi, J. Mei, P.P. Peng, S.H. Luo, Compos. Part B-Eng. 167 (2019) 566–572.
[115] R. Gangopadhyay, A. De, Chem. Mater. 12 (2000) 608–622.
[116] J. Gnanaraj, V. Pol, A. Gedanken, D. Aurbach, Electrochem. Commun. 5 (2003) 940–945.
[117] S.T. Myung, K. Izumi, S. Komaba, Y.K. Sun, H. Yashiro, N. Kumagai, Chem. Mater. 17 (2005) 3695–3704.
[118] F.Y. Lai, X.Y. Zhang, H.Q. Wang, S.Y. Hu, X.M. Wu, Q. Wu, Y.G. Huang, Z.Q. He, Q.Y. Li, ACS Appl. Mater. Interfaces 8 (2016) 21656–21665.
[119] Y. Fan, J. Wang, Z. Tang, W. He, J. Zhang, Electrochim. Acta 52 (2007) 3870–3875.
[120] S.K. Hu, G.H. Cheng, M.Y. Cheng, B.J. Hwang, R. Santhanam, J. Power Sources 188 (2009) 564–569.
[121] C.G. Zhang, X.Y. Liu, Q.L. Su, J.H. Wu, T. Huang, ACS Sustain. Chem. Eng. 5 (2017) 640–647.
[122] D. Arumugam, G.P. Kalaignan, Electrochim. Acta 55 (2010) 8709–8716.
[123] Y.S. Shang, J.L. Liu, T. Huang, A.S. Yu, Electrochim. Acta 113 (2013) 248–255.
[124] S.H. Lee, M.S. Jeong, J.P. Cho, Adv. Energy Mater. 3 (2013) 1623–1629.
[125] Y.P. Wang, X.Y. Wang, S.Y. Yang, H.B. Shu, Q.L. Wei, Q. Wu, Y.S. Bai, B. Hu, J. Solid State Electrochem. 16 (2012) 2913–2920.
[126] S. Zhao, Y. Bai, Q.J. Chang, Y.Q. Yang, W.F. Zhang, Electrochim. Acta 108 (2013) 727–735.
[127] Q.Q. Chen, Y.B. Wang, T.T. Zhang, W.M. Yin, J.W. Yang, X.Y. Wang, Electrochim. Acta 83 (2012) 65–72.
[128] Z.J. Zhang, S.L. Chou, Q.F. Gu, H.K. Liu, H.J. Li, K.S. Ozawa, J.Z. Wang, ACS Appl. Mater. Interfaces 6 (2014) 22155–22165.
[129] C.L. Wei, H.F. Fei, Y.L. An, Y.C. Zhang, J.K. Feng, Electrochim. Acta 309 (2019) 362–370.
[130] F. Kong, X. He, Q. Liu, X. Qi, Y. Zheng, R. Wang, Y. Bai, Ceram. Int. 44 (2018) 11591–11596.
[131] S. Niu, Z. Wang, M. Yu, M. Yu, L. Xiu, S. Wang, X. Wu, J. Qiu, ACS Nano 12 (2018) 3928–3937.
[132] G.M. Song, W.J. Li, Y. Zhou, Mater. Chem. Phys. 87 (2004) 162–167.
[133] H. Zhang, Y.L. Xu, D. Liu, Electrochim. Acta 125 (2014) 225–231.
[134] D. Capsoni, M. Bini, G. Chiodelli, V. Massarotti, M.C. Mozzati, C.B. Azzoni, Solid State Commun. 125 (2003) 179–183.
[135] D. Arumugam, G. Paruthimal Kalaignan, K. Vediappan, C.W. Lee, Electrochim. Acta 55 (2010) 8439–8444.
[136] H.Y. Zhao, X.Y. Gao, Y.F. Li, W. Qi, C.G. Ran, Y.P. Fu, J.T. Feng, X.Q. Liu, J.X.Su. Liu, Ceram. Int. 45 (2019) 17591–17597.
[137] T. Kakuda, K. Uematsu, K.J. Toda, M. Sato, J. Power Sources 167 (2007) 499–503.
[138] T.F. Yi, X.G. Hu, K. Gao, J. Power Sources 162 (2006) 636–643.
[139] S.T. Myung, S. Komaba, N. Kumagai, J. Electrochem. Soc. 148 (2001) A482–A489.
[140] S. Bhuvaneswari, U.V. Varadaraju, R. Gopalan, R. Prakas, Electrochim. Acta 301 (2019) 342–351.
[141] D.Q. Liu, Z.Z. He, Q. Liu, J. Alloys Compd. 440 (2007) 69–73.
[142] D. Capsoni, M. Bini, G. Chidelli, P. Mustarelli, V. Massarotti, C.B. Azzoni, M.C. Mozzati, L. Linati, J. Phys. Chem. B 106 (2002) 7432–7438.
[143] L.L. Xiong, Y.L. Xu, T. Tao, J.B. Goodenough, J. Power Sources 199 (2012) 214–219.
[144] C. Wu, F. Wu, L.Q. Chen, X.J. Huang, Solid State Ionics 152–153 (2002) 335–339.
[145] Z.D. Peng, Q.L. Jiang, K. Du, W.G. Wang, G.R. Hu, Y.X. Liu, J. Alloys Compd. 493 (2010) 640–644.
[146] H.C. Wang, C.H. Lu, J. Power Sources 119–121 (2003) 738–742.
[147] C.Y. Wang, S.G. Lu, S.R. Kan, J. Pang, W.R. Jin, X.J. Zhang, J. Power Sources 189 (2009) 607–610.
[148] S. Mandal, R.M. Rojas, J.M. Amarilla, P. Calle, N.V. Kosova, V.F. Anufrienko, J.M. Rojo, Chem. Mater. 14 (2002) 1598–1605.
[149] X.J. Sun, X.H. Hu, Y. Shi, S.X. Li, Y.Q. Zhou, Solid State Ionics 180 (2009) 377–380.
[150] Y. Xu, G. Chen, E. Fu, M. Zhou, M. Dunwell, L. Fei, S. Deng, P. Andersen, Y. Wang, Q. Jia, H. Luo, RSC Adv. 3 (2013) 18441–18445.
[151] M.A. Kebede, N. Kunjuzwa, C.J. Jafta, M.K. Mathe, K.I. Ozoemena, Electrochim. Acta 128 (2014) 172–177.
[152] Q. Wei, X. Wang, X. Yang, B. Ju, B. Hu, H. Shu, W. Wen, M. Zhou, Y. Song, H. Wu, H. Hu, J. Mater. Chem. A 1 (2013) 4010–4016.
[153] H. Sun, Y. Chen, C. Xu, D. Zhu, L. Huang, J. Solid State Electrochem. 16 (2012) 1247–1254.
[154] D. Arumugam, G.P. Kalaignan, P. Manisankar, Solid State Ionics 179 (2008) 580–586.
[155] M.J. Iqbal, Z. Ahmad, J. Power Sources 179 (2008) 763–769.
[156] R. Thirunkaran, A. Sivashanmugam, S. Gopukumar, R. Rajalakshmi, J. Power Sources 187 (2009) 565–574.
[157] D. Arumugam, G.P. Kalaignan, J. Electroanal. Chem. 648 (2010) 54–59.
[158] C.Q. Xu, Y.W. Tian, Y.C. Zhai, L.Y. Liu, Mater. Chem. Phys. 98 (2006) 532–538.
[159] K.M. Elsabawy, M.M.A. Sekkina, F.G. Elmetwaly, Solid State Sci. 13 (2011) 601–606.
[160] R. Singhal, S.R. Das, M.S. Tomar, O. Ovideo, S. Nieto, R.E. Melgarejo, R.S. Katiyar, J. Power Sources 164 (2007) 857–861.
[161] D.K. Lee, S.C. Han, D. Ahn, S.P. Singh, K.S. Sohn, M. Pyo, ACS Appl. Mater. Interfaces 4 (2012) 6842–6848.
[162] S.R.K. Balaji, D. Mutharasu, S. Shanmugan, N.S. Subramanian, K. Ramanathan, Ionics 16 (2010) 351–360.
[163] H.W. Liu, K.L. Zhang, Mater. Lett. 58 (2004) 3049–3051.
[164] W. Choi, A. Manthiram, J. Electrochem. Soc. 154 (2007) A792–A797.
[165] W. Choi, A. Manthiram, J. Electrochem. Soc. 154 (2007) A614–A618.
[166] W.R. Liu, S.H. Wu, H.S. Sheu, J. Power Sources 146 (2005) 232–236.
[167] Z.F. Dong, Y.D. Huang, D.Z. Jia, Z.P. Guo, J. Solid State Electrochem. 15 (2011) 725.
[168] D. Liu, W. Zhu, J. Trottier, C. Gagnon, F. Barray, A. Guerfi, A. Mauger, H. Groult, C.M. Julien, J.B. Goodenough, K. Zaghib, RSC Adv. 4 (2014) 154–167.
[169] K. Muharrem, F.A. Jarar, G.A. Glenn, Chem. Mater. 18 (2006) 3585–3592.
[170] A. Manthiram, K. Chemelewski, E. Lee, Energy Environ. Sci. 7 (2014) 1339–1350.
[171] L. Wang, H. Li, X. Huang, E. Baudrin, Solid State Ionics 193 (2011) 32–38.
[172] D. Aurbach, J. Power Sources 89 (2000) 206–218.
[173] E. Wang, D. Ofer, W. Bowden, N. Iltchev, R. Moses, K. Brandt, J. Electrochem. Soc. 147 (2000) 4023–4028.
[174] L. Yang, M. Takahashi, B. Wang, Electrochim. Acta 51 (2006) 3228–3234.
[175] N.P.W. Pieczonka, Z. Liu, P. Lu, K.L. Olson, J. Moote, B.R. Powell, J.H. Kim, J. Phys. Chem. C 117 (2013) 15947–15957.
[176] N. Arun, V. Aravindan, S. Jayaraman, N. Shubha, W.C. Ling, S. Ramakrishna, S. Madhavi, Nanoscale 6 (2014) 8926–8934.
[177] J. Liu, W. Liu, S.M. Ji, Y.C. Zhou, P. Hodgson, Y.C. Li, ChemPlusChem 78 (2013) 636–641.
[178] H.-M. Cho, M.V. Chen, A.C. MacRae, Y.S. Meng, ACS Appl. Mater. Interfaces 7 (2015) 16231–16239.
[179] X.L. Zhang, F.Y. Cheng, J.G. Yang, J. Chen, Nano Lett. 13 (2013) 2822–2825.
[180] W.W. Sun, Y.J. Li, K. Xie, S.Q. Luo, G. Bai, X. Tan, C.M. Zheng, Nano Energy 54 (2018) 175–183.
[181] H.B. Lin, Y.M. Zhang, H.B. Rong, S.W. Mai, J.N. Hu, Y.H. Liao, L.D. Xing, M.Q. Xu, X.P. Li, W.S. Li, J. Mater. Chem. A 2 (2014) (1995) 11987–11991.
[182] J. Wang, W. Lin, B. Wu, J. Zhao, Electrochim. Acta 145 (2014) 245–253.
[183] Z. Yang, Y. Jiang, J.H. Kim, Y. Wu, G.L. Li, Y.H. Huang, Electrochim. Acta 117 (2014) 76–83.
[184] C. Locati, U. Lafont, L. Simonin, F. Ooms, E. Kelder, J. Power Sources 174 (2007) 847–851.
[185] M.C. Yang, B. Xu, J.H. Cheng, C.J. Pan, B.J. Hwang, Y.S. Meng, Chem. Mater. 23 (2011) 2832–2841.
[186] M.W. Jang, H.G. Jung, B. Scrosati, Y.K. Sun, J. Power Sources 220 (2012) 354–359.
[187] G.B. Zhong, Y.Y. Wang, Z.C. Zhang, C.H. Chen, Electrochim. Acta 56 (2011) 6554–6561.
[188] T.F. Yi, J. Shu, Y.R. Zhu, A.N. Zhou, R.S. Zhu, Electrochem. Commun. 11 (2009) 91–94.
[189] T.F. Yi, J. Shu, Y.R. Zhu, R.S. Zhu, J. Phys. Chem. Solids 70 (2009) 153–158.
[190] J. Liu, A. Manthiram, J. Phys. Chem. C 113 (2009) 15073–15079.
[191] D.W. Shin, A. Manthiram, Electrochem. Commun. 13 (2011) 1213–1216.
[192] M. Bini, P. Boni, P. Mustarelli, I. Quinzeni, G. Bruni, D. Capsoni, Solid State Ionics 320 (2018) 1–6.
[193] H. Wang, T.A. Tan, P. Yang, M.O. Lai, L. Lu, J. Phys. Chem. C 115 (2011) 6102–6110.
[194] J.H. Kim, N.P.W. Pieczonka, Y.K. Sun, B.R. Powell, J. Power Sources 262 (2014) 62–71.
[195] J.N. Zhang, G. Sun, Y. Han, F.D. Yu, X. Qin, G. Shao, Z.B. Wang, Electrochim. Acta 343 (2020) 136105.
[196] T.F. Yi, Y. Xie, Y.R. Zhu, R.S. Zhu, M.F. Ye, J. Power Source 211 (2012) 59–65.
[197] S.J.R. Prabakar, S.C. Han, S.P. Singh, D.K. Lee, K.S. Sohn, M. Pyo, J. Power Sources 209 (2012) 57–64.
[198] T.F. Yi, B. Chen, Y.R. Zhu, X.Y. Li, R.S. Zhu, J. Power Sources 247 (2014) 778–785.
[199] G. Du, Y.N. Li, J. Yang, J. Wang, Mater. Res. Bull. 43 (2008) 3607–3613.
[200] T.F. Yi, S.Y. Yang, X.Y. Li, J.H. Yao, Y.R. Zhu, R.S. Zhu, J. Power Sources 246 (2014) 505–511.
[201] W. Tao, M.L. Xu, Y.R. Zhu, Q.Y. Zhang, T.F. Yi, Sci. China Mater. 60 (2017) 728–738.
[202] Y. Yu, M. Xiang, J. Guo, C. Su, X. Liu, H. Bai, W. Bai, K. Duan, J. Colloid Interface Sci. 555 (2019) 64–71.

[203] T.F. Yi, H.P. Liu, Y.R. Zhu, L.J. Jiang, Y. Xie, R.S. Zhu, J. Power Sources 215 (2012) 258–265.
[204] T.F. Yi, Y.M. Li, X.D. Cai, S.Y. Yang, Y.R. Zhu, Mater. Today Energy 4 (2017) 25–33.
[205] T.F. Yi, C.Y. Li, Y.R. Zhu, J. Shu, R.S. Zhu, J. Solid State Electrochem. 13 (2009) 913–919.
[206] T.F. Yi, L.C. Yin, Y.Q. Ma, H.Y. Shen, Y.R. Zhu, R.S. Zhu, Ceram. Int. 39 (2013) 4673–4678.
[207] T.F. Yi, Y. Xie, J. Shu, Z.H. Wang, C.B. Yue, R.S. Zhu, H.B. Qiao, J. Electrochem. Soc. 158 (2011) A266–A274.
[208] T.F. Yi, Y. Xie, L.J. Jiang, J. Shu, C.B. Yue, A.N. Zhou, M.F. Ye, RSC Adv. 2 (2012) 3541–3547.
[209] C. Gao, H.P. Liu, S.F. Bi, S.S. Fan, H. Xi, Q.Y. Meng, C.X. Luo Li, J. Mater. 6 (2020) 712–722.
[210] N. Zhang, T. Yang, Y. Lang, K. Sun, J. Alloy. Compd. 509 (2011) 3783–3786.
[211] Y. Kwon, Y. Lee, S.O. Kim, H.S. Kim, K.J. Kim, D.J. Byun, W.C. Choi, ACS Appl. Mater. Interfaces 10 (2018) 29457–29466.
[212] X.W. Gao, Y.F. Deng, D. Wexler, G.H. Chen, S.L. Chou, H.K. Liu, Z.C. Shi, J.Z. Wang, J. Mater. Chem. A 3 (2015) 404–411.
[213] U. Nisar, S.A. Al-Hail, R.K. Petla, R.A. Shakoor, R. Essehli, R. Kahraman, S.Y. AlQaradawi, D.K. Kim, I. Belharouak, M.R. Amin, ACS Appl. Energy Mater. 2 (2019) 7263–7271.
[214] T.F. Yi, X. Han, B. Chen, Y.R. Zhu, Y. Xie, J. Alloy. Compd. 703 (2017) 103–113.
[215] Q. Chang, A.J. Wei, W. Li, X. Bai, L.H. Zhang, R. He, Z.F. Liu, Ceram. Int. 45 (2019) 5100–5110.
[216] J. Guo, Y.J. Li, Y.X. Chen, S.Y. Deng, J. Zhu, S.L. Wang, J.P. Zhang, S.H. Chang, D. W. Zhang, X.M. Xi, J. Alloy. Compd. 811 (2019) 152031.
[217] S. Tao, F.J. Kong, C.Q. Wu, X.Z. Su, T. Xiang, S.M. Chen, H.H. Hou, L. Zhang, Y. Fang, Z.C. Wang, W.S. Chu, B. Qian, L. Song, J. Alloy. Compd. 705 (2017) 413–419.
[218] F. Ma, F.S. Geng, A.B. Yuan, J.Q. Xu, Phys. Chem. Chem. Phys. 19 (2017) 9983–9991.
[219] J.J. Pan, B. Chen, Y. Xie, N. Ren, T.F. Yi, Mater. Lett. 253 (2019) 136–139.
[220] J.R. Mou, Y.L. Deng, L.H. He, Q.J. Zheng, N. Jiang, D.M. Lin, Electrochim. Acta 260 (2018) 101–111.
[221] C.T. Chu, A. Mondal, N.V. Kosova, J.Y. Lin, Appl. Surf. Sci. 530 (2020) 147169.
[222] C.Y. Yu, L. Dong, Y.X. Zhang, K. Du, M.M. Gao, H.L. Zhao, Y. Bai, Solid State Ionics 357 (2020) 115464.
[223] Y.P. Li, D.D. Wang, T.H. Xu, M.Y. Wu, D. Pan, H.L. Zhao, Y. Bai, Solid State Ionics 324 (2018) 7–12.
[224] T.F. Yi, Y.M. Li, X.Y. Li, J.J. Pan, Q.Y. Zhang, Y.R. Zhu, Sci. Bull. 62 (2017) 1004–1010.
[225] Y.D. Wu, L.B. Ben, H.L. Yu, W.B. Qi, Y.J. Zhan, W.W. Zhao, X.J. Huang, ACS Appl. Mater. Interfaces 11 (2019) 6937–6947.
[226] T.H. Xu, Y.P. Li, D.D. Wang, M.Y. Wu, D. Pan, H.L. Zhao, Y. Bai, ACS Sustain. Chem. Eng. 6 (2018) 5818–5825.
[227] H.M. Wu, I. Belharouak, A. Abouimrane, Y.K. Sun, K. Amine, J. Power Sources 195 (2010) 2909–2913.
[228] H. Hu, Q. Chen, Z.J. Chen, H.Y. Chen, Appl. Surf. Sci. 316 (2014) 348–354.
[229] H. Kim, D.J. Byun, W.Y. Chang, H.G. Jung, W.C. Choi, J. Mater. Chem. A 5 (2017) 25077–25089.
[230] Y.R. Zhu, T.F. Yi, X.Y. Li, Y. Xie, S.H. Luo, Mater. Lett. 239 (2019) 56–58.
[231] X.J. Yang, T. Yang, S.S. Liang, X. Wu, H.P. Zhang, J. Mater. Chem. A 8 (2014) 10359–10364.
[232] Y.L. Deng, J.R. Mou, H.L. Wu, N. Jiang, Q.J. Zheng, K.H. Lam, C.G. Xu, D.M. Lin, Electrochim. Acta 235 (2017) 19–31.
[233] J.R. Mou, Y.L. Deng, Z.C. Song, Q.J. Zheng, K.H. Lam, D.M. Lin, Dalton T. 47 (2018) 7020–7028.
[234] H. Deng, P. Nie, H. Luo, Y. Zhang, J. Wang, X. Zhang, J. Mater. Chem. A 8 (2014) 18256–18262.
[235] Y. L, Z.P. Lu, C.F. Deng, J.J. Ding, Y. Xu, X.J. Lu, G. Yang, J. Mater. Chem. A 5 (2017) 996-1004.
[236] J.Z. Zhao, Y.R. Liu, Y. He, K. Lu, J. Alloy. Compd. 779 (2019) 978–984.